Using the Pythonic Direct Data Assimilation (PyDDA) Framework for Dual-Doppler Wind Retrievals of Idealized Downburst Outflows

Katherine Simzer

Department of Atmospheric & Oceanic Sciences
McGill University
Montréal, Québec, Canada

July 27, 2023

A thesis presented for the degree of Masters of Atmospheric Sciences

Abstract

Radar observations and our utilization of radar as a weather forecasting tool have come a long way since they were first developed in the 1930s, but there are inherent limitations in the radar data. In general, surface and near-surface winds are challenging to record using Doppler radars due to the ground clutter, surface obstacles and topography, and Earth's curvature effects, to name a few factors. This creates issues for the forecasting and research of thunderstorm downbursts, whose outflows occur at these lower altitudes and interact directly with human activity. Downbursts are negatively buoyant downdrafts that emerge from a thunderstorm and spread outward upon hitting the surface. The maximum wind speeds in downburst outflows can exceed 70 m/s and they are usually observed in the region 50–150 m above the ground. To better understand these phenomena, downbursts are often studied using impinging jet models in wind tunnels and numerical models. Using the principles of similitude, a small-scale downburst-like impinging jet produced in a wind tunnel can be scaled up to represent a full-sized downburst outflow. In our work, data of a fully scaled impinging jet modelled using an analytical model is provided to Pythonic Direct Data Assimilation

Framework (PyDDA) from two virtual radars that are located perpendicular to each other with the downburst model in the centre. The PyDDA is a data assimilation framework developed for the retrieval of high-resolution three-dimensional wind fields from an arbitrary number of Doppler radars. The ability of PyDDA to interpolate missing near-surface data is evaluated to gauge its versatility in the modelling of idealized downburst outflows with limited radar data.

Résumé

Les observations radar et l'utilisation du radar comme outil de prévision météorologique ont beaucoup progressées depuis leur création dans les années 1930. Les données radar présentent cependant des limites inhérentes. En effet, il est en général difficile d'évaluer les vents de surface et les vents proches de la surface à l'aide des radars Doppler en raison des échos parasites du sol, des obstacles de surface et de la topographie, ainsi que des effets de la courbure de la Terre, pour ne citer que quelques facteurs. Cela pose donc des problèmes pour la prévision et la recherche sur les rafales descendantes d'orages dont les vents qui s'écoulent d'un orage se produisent à des altitudes plus basses et interagissent directement avec l'activité humaine. Les rafales descendantes sont des courants descendants à flottabilité négative qui émergent d'un orage et s'étendent vers l'extérieur lorsqu'ils atteignent la surface. La vitesse maximale du vent dans les rafales descendantes peut dépasser 70 m/s et celles-ci sont généralement observées dans les régions situées entre 50 et 150 m au-dessus du sol. Pour mieux comprendre ces phénomènes, les rafales descendantes sont souvent étudiées à l'aide de modèles de jets d'impacts en soufflerie et de modèles numériques. En utilisant les principes de similitude, un jet d'impact à petite échelle de type rafale descendante produit dans une soufflerie peut être mis à l'échelle pour représenter un écoulement de rafale descendante de taille normale. Dans notre travail, les données d'un jet d'impact à échelle complète modélisé à l'aide d'un modèle analytique sont fournies au cadre d'assimilation de données directes Pythonic (PyDDA) à partir de deux radars virtuels situés perpendiculairement l'un à l'autre avec le modèle de rafale descendante au centre. PyDDA est un cadre d'assimilation de données développé pour le recouvrement de champs de vent tridimensionnels à haute résolution à partir d'un nombre arbitraire de radars Doppler. La capacité de PyDDA à interpoler les données manquantes près de la surface est évaluée afin de mesurer sa polyvalence dans la modélisation des écoulements de rafales descendantes avec des données radar limitées.

Acknowledgements

First and foremost, I would like to thank my supervisor Professor Djordje Romanic as this thesis work would not have been possible without his support and guidance.

Robert Jackson and the rest of the PyDDA contributors also deserve thanks for their tireless work developing the software that made this project possible.

I would like to thank the Department of Atmospheric and Oceanic Sciences (AOS) at McGill for setting the foundation of my studies through their classes and programs over the last seven years. My experience in the Bachelor of Physics & Atmospheric Sciences program provided me with the knowledge and experience to make this work possible.

Further, I would like to gratefully acknowledge the support of Professor Gregory Lewis at Ontario Tech University to whom I owe my first research experience after my second year of my Bachelor's studies. He provided an invaluable positive experience that opened my eyes to the possibilities of academic research and which surely influenced my later path in academia.

I would like to thank my family and friends for their support over the last seven years to get me to this point, as this would not have been possible without them. I would especially like to thank my cat, who was always there to make me smile and provide comfort and companionship.

Thank you to Professor Frédéric Fabry for taking the time to review this thesis and provide helpful comments to improve it.

Finally, I would like to dedicate this work to the great academics whose initial discoveries made this thesis possible. Poreh, Fujita, and Hjelmfelt to name a few, laid the groundwork to this thesis many decades ago. Their contributions to science and the study of downbursts carry on today.

Contribution of Authors

In this thesis, I (Katherine Simzer) developed the code and calculations used for the model following the methodology explained in Chapter 2. I produced the figures and results found in Chapter 3 as well as the analysis, interpretation, and discussion of said results. I wrote the text of the thesis and prepared the review of relevant literature.

The research topic was conceptualized by my supervisor, Professor Djordje Romanic. He provided supervision and guidance throughout the project as well as funding acquisition, literature suggestions, and contributed to the editing of this thesis.

Contents

List of Figures

List of Tables

Nomenclature

AGL Above Ground Level.

CEDRIC Custom Editing and Display of Reduced Information in Cartesian space.

CINDE Convection Initiation and Downburst Experiment.

COHMEX Cooperative Huntsville Meteorological Experiment.

DDA Dual Doppler Analysis.

FLOWS Federal Aviation Administration/Lincoln Lab Operational Weather Studies.

JAWS Joint Airport Weather Studies.

MIST Microburst and Severe Thunderstorm Project.

NIMROD Northern Illinois Meteorological Research on Downbursts.

PyDDA Pythonic Direct Data Assimilation.

RMS Root Mean Square.

Chapter 1

Introduction

First developed in the 1930s, radar observations and our utilization of radar as a tool for weather forecasting and diagnostics have advanced greatly since their inception. Despite this, there will always be limitations in the radar data that can be retrieved that lies in the geometry of radar observations. For example, due to the typical values of elevation angles of the radar beam, no surface winds can be recorded. This issue is because as the radar beam gets further away from the radar, the higher in altitude the beam is above the surface. The logical solution to this would be to lower the radar beam, but the interference of radar beams close to the ground from objects such as trees, mountains, or buildings, limits how low of an angle a radar beam can be successfully deployed. A diagram of this can be seen in Figure 1.1, showing the relationship between the elevation angle of the radar beam and how it might interact with an idealized thunderstorm. There are further issues in retrieving low-level data from radars that are not shown in this figure, including the interactions of ground clutter and the furthering of the distance between the radar beam and the surface of the Earth as one moves further away from the radar due to the curvature of the Earth.

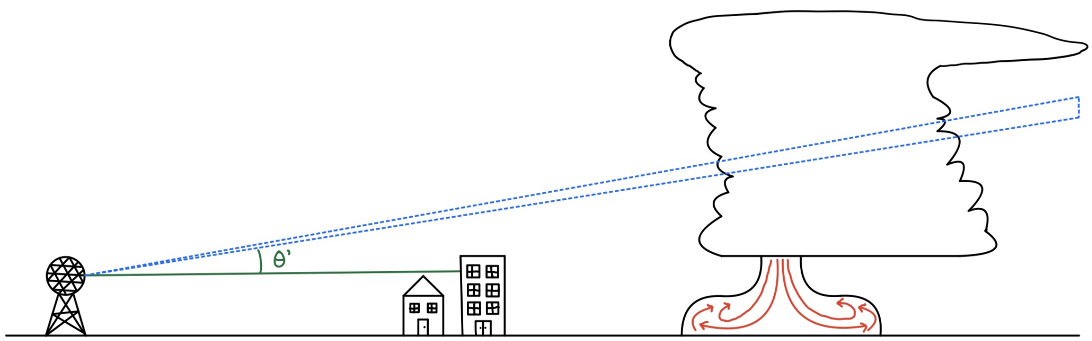

Figure 1.1: Diagram of the geometry of a radar beam (blue) directed towards an idealized downburst-producing thunderstorm. The elevation angle $\theta' = 0°$ (green) would cause interference between the beam and the buildings.

Despite these shortcomings, radar measurements are a very useful tool in the forecasting of severe weather events such as thunderstorms. Nonetheless, we are unable to see radar data from these storms at lower altitude levels where they most directly interact with human activity. Improving our understanding of thunderstorm dynamics at lower elevations, especially when it comes to thunderstorm downbursts, for example, will aid in the understanding and forecasting of potential impacts associated with thunderstorm downbursts.

In the study done by Hadavi et al. (2022), 47 catastrophic wind events were identified over the Canadian provinces of Ontario and Québec over the period of 2008-2021. Using the database hosted and maintained by the Toronto-based insurance firm Catastrophe Indices and Quantification Inc. (CatIQ), the total imposed wind losses were more than CA$5.2 billion with about 67% coming from convective storms ($3.5 billion). These numbers highlight the need for more research on these wind storms, as the current building codes and wind loading recommendations are based on large-scale synoptic winds (Hadavi et al., 2022).

1.1 The History and Discovery of Downbursts

As with many natural phenomena that humans have discovered, thunderstorm downbursts have been happening for much longer than when they were first named and identified. In scientific literature, the term "downburst" was first coined by Fujita and Byers in 1977. They recognized an instance of a particularly strong thunderstorm downdraft, which lead to an airplane crashing just short of the runway at John F. Kennedy International Airport in New York in June of 1975 (Fujita and Byers, 1977). They defined a downburst as "a localized, intense downdraft with vertical currents exceeding a downward speed of 12 ft s^{-1} at 300 ft above the surface" (Fujita and Byers, 1977). In their paper, they tied the instance of these "downbursts" to overshooting tops of clouds above the anvil, and a "spearhead echo" signature on radar observations. In the years following this discovery, research on the phenomena of downbursts increased, with Fujita continuing to contribute greatly to this field.

The term “microburst” was first specified in Fujita’s work with project NIMROD (Northern Illinois Meteorological Research on Downbursts) in 1978–79, where it was used to differentiate between smaller and larger downbursts based on the diameter of the damage they caused on the ground (Fujita, 1978). Fujita defined microscale downbursts (microbursts) to have an outflow diameter of less than 3 miles (1978).

When it comes to the naming conventions that are used today, Fujita proposed a standardized scale that follows the order of the vowels in the alphabet: maso, meso, miso, moso and muso, which are scaled to the size of a given planet via its equatorial length (Fujita, 1981). Following this scale, he shows downbursts straddling the meso- and misoscales, specifying that microbursts belong to the misoscale with a diameter of damage that is less than 4 km. It is in his later work that the term “macroburst” was defined to specify a downburst with a diameter of damage greater than 4 km (Fujita, 1985).

During the period from 1978–87, multiple field campaigns were deployed to collect data and learn more about the fascinating phenomenon of the downburst coined by Fujita and Byers (1977). The first of these campaigns was the Northern Illinois Meteorological Research on Downbursts (NIMROD) beginning in May of 1978. Using a triple–Doppler radar network in Northern Illinois, this field work was the first time that microbursts were detected by a Doppler radar (Fujita, 1985). The NIMROD field campaign in Northern Illinois turned into the National Intensive Meteorological Research on Downbursts for the widespread collection of damage survey data in 1978 and 1979 (Fujita, 1978). In the summer of 1982, the Joint

Airport Weather Studies (JAWS) field campaign investigated the kinematics of downbursts using three radars as well: one S– (10 cm) and two C–band (5 cm) Doppler radars at and surrounding the Denver International Airport in Denver, Colorado (McCarthy et al., 1982). In the summers of 1985 and 1985, the Federal Aviation Administration/Lincoln Lab Operational Weather Studies (FLOWS) field campaign took place, coinciding in part with the Microburst and Severe Thunderstorm Project (MIST) of 1986 (Wolfson et al., 1987; Atkins and Wakimoto, 1991). The two field campaigns were colocated near Huntsville, Alabama for June and July of 1986 as part of the Cooperative Huntsville Meteorological Experiment (COHMEX; Wolfson et al., 1987). In the summer of 1987, another field campagin took place in Denver, Colorado. This was the Convection Initiation and Downburst Experiment (CINDE), which used 6 Doppler radars, 87 mesonet stations, and 3 research aircraft among other instruments (Wilson et al., 1988). Each of these field campaigns brought important information and data to light on the subject of thunderstorm downbursts. Since this period of large-scale field campaigns, no further comparable studies have been done.

1.2 Downburst Structure

The first look into downburst structure was, naturally, through the damage left behind on the ground. This signature was what first signalled to Fujita that a different phenomenon from a tornado was occurring. When aerially assessing the damage left behind from the super-outbreak of 148 tornadoes that occurred on 3–4 of April 1974, Fujita noticed a pattern of damage that did not resemble the typical swirling patterns of fallen trees that he was used to observing (Fujita, 1985). Near Beckley, West Virginia, he noticed hundreds of trees blown down outward in a “starburst pattern” (Fujita, 1985). When all of the surveying of the super-outbreak was complete, Fujita remarked that “at least 15 percent of the path lengths were caused by outburst winds, rather than tornado winds” (Fujita, 1985).

When analyzing the outburst pattern that he was seeing, Fujita remarked that it was natural to visualize the jet of a downdraft hitting the surface at the centre of the starburst pattern and spreading outwards (Fujita, 1985). This idea was controversial at the time, as most meteorologists believed that no matter how strong a downdraft may be, it should weaken to an insignificant speed long before reaching the surface (Fujita, 1985). The multiple field campaigns taking place from 1978–1986 sought to further understand the cause and structure of the phenomenon causing these “starburst” damage patterns.

Using the data collected from NIMROD and JAWS, Fujita recognized two different types of microbursts (Fujita, 1985). A microburst that has a strong downdraft and outflow was declared to be an “outflow microburst”. Based on observational data, Fujita noted that slow-travelling outflow microbursts are often encircled by a vortex ring (shown in Fig. 1.2). This vortex ring keeps stretching until it reaches the limit where it breaks into several pieces of separate roll vortices. If one of these roll vortices becomes a runaway, it can leave behind its own narrow field of damage and is known as a “rotor microburst” (Fujita, 1985). The schematics of both outflow and rotor microbursts are shown in Fig. 1.2, with the dotted lines along the ground of the outflow microburst representing the areas where the vortex ring breaks apart.

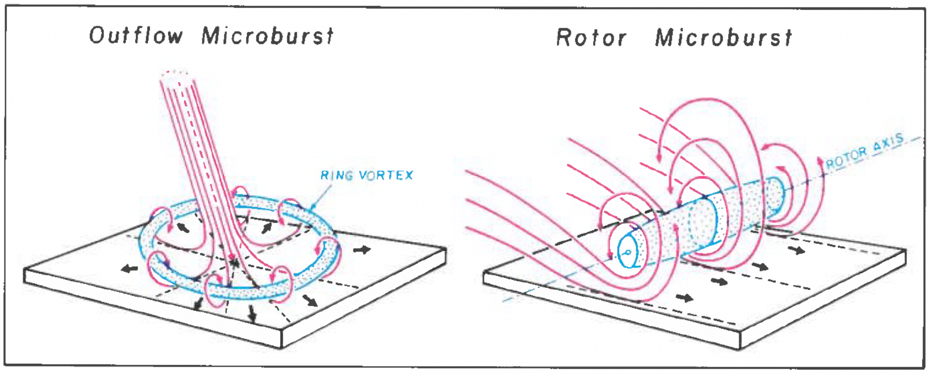

Figure 1.2: Schematic of the outflow and rotor microbursts. The outflow microbursts are the most common. Figure taken from Fujita (1985).

The schematic of the outflow microburst in Fig. 1.2 does not show any rotation along the downdraft, but the data collected by the JAWS Doppler radars showed the wind field aloft to be rotating at the height of the downflow (Fujita, 1985). However, JAWS did confirm that misocyclones exist in the downflow region of outflow microbursts. This rotation is shown in the schematic of Fig. 1.3.

These studies on the structure of downbursts lead to the classifications that we still use today to differentiate between a micro– and a macroburst. Fujita declared a macroburst to have its outburst winds extending more than 4 km in diameter, with damaging winds that last 5–30 minutes at speeds of up to 60 m s^{-1} (Fujita, 1985). A microburst, on the other hand, has outburst winds extending less than 4 km in diameter, with damaging winds that last up to 10 minutes and can reach speeds of up to 75 m s^{-1} (Fujita, 1985).

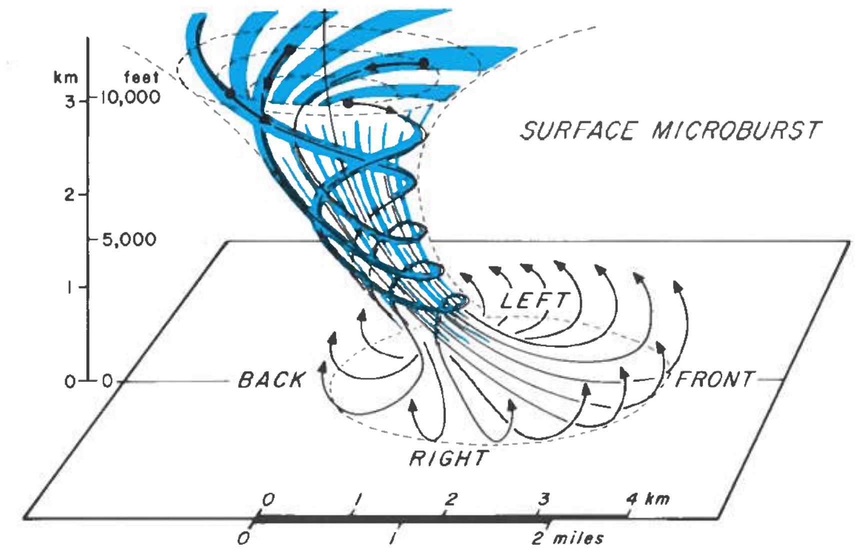

Figure 1.3: Schematic of a surface microburst with a damage radius of 4 km and a misocyclone aloft. Most misocyclones rotate cyclonically though exceptional ones can rotate anticyclonically. Figure taken from Fujita (1985).

Although Fujita started much of this work on the structural aspects of downburst outflows, additional research was done as a result of the JAWS field campaign by Hjelmfelt (Hjelmfelt, 1988). While Fujita's schematics did not include too much in the way of the specific values other than a general scale (see Fig. 1.3), Hjelmfelt included average values measured from 26 microburst outflows during the JAWS campaign for the diameter of the downdraft, the radius measured from the centre where the maximum velocity occurred at the surface, the depth of the outflow, and the velocity of the downdraft, among other parameters (Hjelmfelt, 1988). Details on the measurements from each downburst can be found in Table 1 of Hjelmfelt (1988). The average values of the measurements can be seen in Fig. 1.4, with a downdraft diameter of 1.8 km, a maximum vertical velocity of 12 m s^{-1}

at an altitude of 1.5 km, and an outflow depth of 0.7 km.

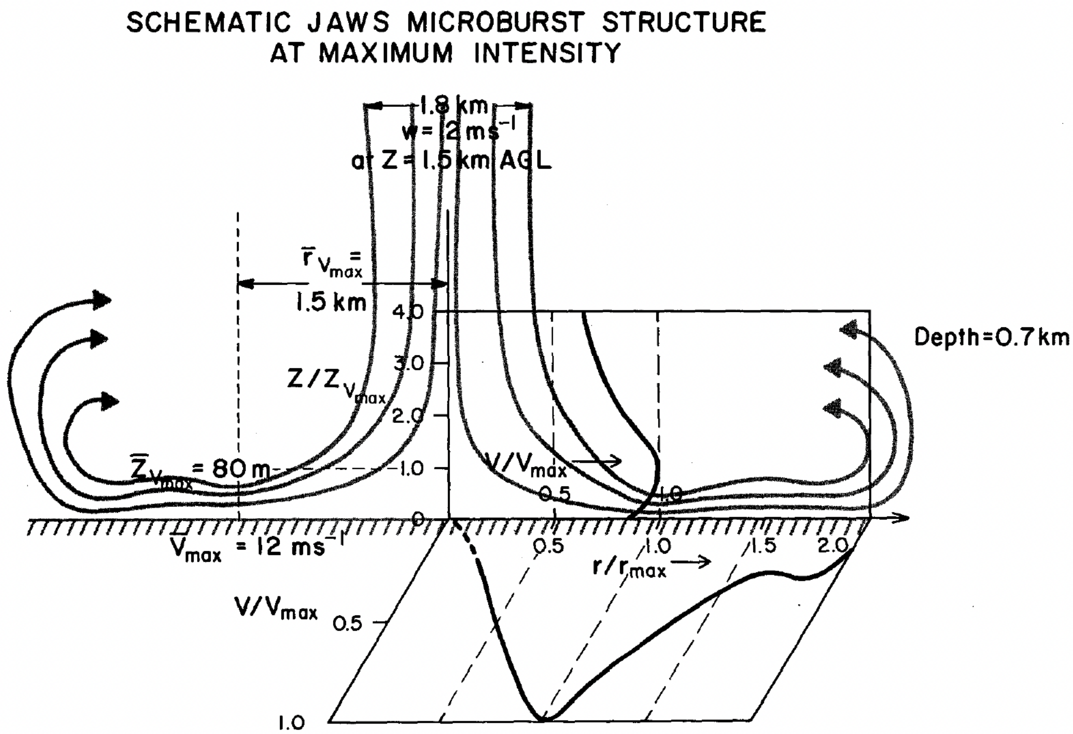

Figure 1.4: Structure of the outflow at the time of maximum intensity and average values of characteristic structural features. Figure taken from Hjelmfelt (1988).

Hjelmfelt also gained more specific insight into the time scale of these microburst outflows. He noted that the intensification of the microbursts from the initially observed divergence took about 7.5 minutes to reach the maximum observed radial velocity differential (Hjelmfelt, 1988). Further, the outflows observed reached microburst intensity about 5 minutes before their maximum outflow intensity. The average time from maximum intensity to decay was around 8 minutes, giving a lifespan of about 13 minutes at microburst intensity or 16 minutes from the initially observed divergence (Hjelmfelt, 1988).

1.3 Downburst Detection and Forecasting

Learning more about the structure and life cycle of thunderstorm downbursts is important for many reasons. Understanding the phenomena itself allows us to understand the kinematics of its formation and improves our ability to forecast them. Knowing more about their structure is also important for wind engineering purposes in terms of wind loading and the wind–structure interaction of downbursts, which allows us to build more resilient structures that are less prone to damage. Due to the short life span and small size of thunderstorm downbursts, they are rarely captured in standard meteorological measurements and high-frequency anemometer measurements of downburst are particularly scarce.

The first work done on detecting thunderstorm downbursts on a radar screen was by Fujita within the project NIMROD. Here he observed an arc–shaped gust front on the Doppler radar accompanied by an extensive positive or negative velocity field behind the gust front (Fujita, 1985). Through the data collected during project NIMROD, Fujita showed the “bow echo” as an inducer of strong micro– and macrobursts. Later in his work, Fujita revised this earlier hypothesis (Fujita, 1978) to hypothesize that the downburst produced the bow echo (Wilson and Wakimoto, 2001).

Before radar detection is possible, forecasters can assess the environment to determine whether or not it is primed to support the formation of thunderstorms producing downbursts. A relatively dry environment over land in the mid–latitudes where the potential for evaporative cooling is high supports the development of strong downdrafts

(Bluestein, 2013). This does not, however, account for the differences in the development of dry and wet downbursts, which are caused by different processes. Dry microbursts often form over arid terrain at an altitude where the environmental lapse rate is almost dry adiabatic and the boundary layer air is dry (Bluestein, 2013). This environment supports intense evaporative cooling as water droplets can fall through unsaturated air for a long time, to the point where they can evaporate completely (Bluestein, 2013). Wet microbursts require a moist environment with a low cloud base that is not conducive to evaporative cooling at low altitudes (Bluestein, 2013). These types of microbursts depend on water loading in intense precipitation to create negative buoyancy, or some evaporative cooling aloft (Bluestein, 2013). The melting of ice particles falling downward through an area of precipitation causes cooling that can also increase the negative buoyancy in both dry and wet microbursts (Bluestein, 2013).

1.4 Modelling Downburst Outflows

With the various field campaigns of 1978–86 providing data for many unique downburst events, further analysis of the new phenomena of downbursts was possible using modelling. This began with two different types of models: meteorologists intended to replicate the dynamics of downbursts based on real events, and the aviation industry desired more simple kinematic models that would allow flight simulators to replicate the wind shear conditions (Burlando and Romanic, 2021). As this research focuses on the interaction of downburst outflows with the Earth's surface, a full, dynamic model is not required.

In its simplest form, a downburst outflow can be modelled by the interaction of a steady impinging jet flow with a flat plate, neglecting buoyancy and with or without friction (Burlando and Romanic, 2021). This type of model is based on the high-pressure touchdown that has been measured and recorded during the mature stage of thunderstorms as early as 1949 with the Thunderstorm Project (Byers and Braham, 1949). This model is more commonly known as an impinging jet model (Zhu and Etkin, 1985), and can be physically simulated in wind chambers or wind tunnels to allow for much easier data collection than conducting field measurements (Burlando and Romanic, 2021).

The impinging jet model chosen for this work was that of Poreh et al. (1967). In this paper, Poreh et al. synthesized several physical experiments of isothermal impinging jets and proposed a set of equations to model the radial wall jet region of an impinging jet. A schematic of the experimental setup is shown in Fig. 1.5. The top orifice of diameter D accelerated air downwards to the flat plate below. Below the orifice, the transition zone of height of approximately $9D$ is seen, with the circular jet region below it. Interacting with the surface are the deflection zone and the radial wall region of the impinging jet flow. The radial wall jet is the region of the developed outflow. To the furthest right-hand side in Fig. 1.5, the vertical velocity profile found in the region of the radial wall jet is schematized. The nose-like profile has a maximum velocity of U_m.

Poreh et al. derived the equations describing the radial wall jet as it was found to

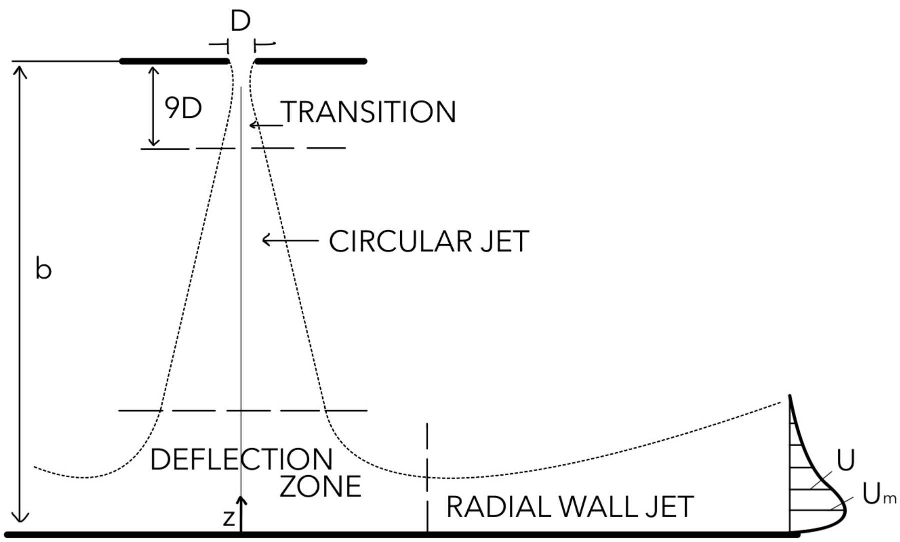

Figure 1.5: Schematic description of the experimental setup used by Poreh et al (1967). Figure adapted from Poreh et al. (1967).

be self–similar (Poreh et al., 1967). This is not the case for the deflection zone, where turbulence causes a lack of self–similarity. In the deflection zone, which is also known as the stagnation region, the velocity and kinetic energy of the flow decreases as it approaches the surface (Bolek and Bayraktar, 2018; Yao et al., 2015). Due to this decrease in velocity in the deflection zone, it is the radial wall jet that is associated with the strongest horizontal winds. For this research, we are interested in the winds that have the highest potential to cause the most damage on the surface, which is in the region of the radial wall jet. For this reason, the model used for this research will not account for the innermost area of the impinging jet model, where the radius outwards from the centre of the model is less than D, the diameter of the orifice (Wood et al., 2001). As for the outer extent of the model, only the area less than $4D$ will be considered (Wood et al., 2001). More information about the specific numbers and equations used can be found in Section 2.1.

1.5 Wind Retrievals

Constructing three–dimensional wind retrievals can give insight into different processes and natural phenomena by combining data from multiple sources. Amalgamating data from different spacial and temporal scales allows the information from each source to play a role in the final wind retrieval solution. This has commonly been done through two different frameworks (Jackson et al., 2020). The first is done by integrating the mass continuity equation from the surface to the top of the atmosphere in order to impose a strong constraint (Gal-Chen, 1978; Gal-Chen and Kropfli, 1984), and the other is the 3D variational (3DVAR) framework (Gao et al., 1999b; Shapiro et al., 2009; Potvin et al., 2012a; Potvin et al., 2012b). The 3DVAR framework minimizes the sum of cost functions relating to each source of data given, which makes it easier to add different sources than in the strong constraint framework. As it is also less sensitive to initial and boundary conditions, the 3DVAR framework is the standard choice for three–dimensional wind retrievals today (Jackson et al., 2020).

Two different software have been historically used to create three-dimensional wind retrievals: Custom Editing and Display of Reduced Information (CEDRIC) and MultiDop (Jackson et al., 2020). CEDRIC uses the strong constraint framework and was written in Fortran 77 and C, which makes it difficult to use (Miller and Fredrick, 1998). MultiDop implements the 3DVAR framework through the Dual Doppler Analysis (DDA) technique (Lang et al., 2017). MultiDop functions as a Python-based interface around the C-based program, but it can be difficult to compile and has limitations for the number of radars that can be implemented into the retrieval.

For these reasons, the Pythonic Direct Data Assimilation (PyDDA) Framework was developed to create a fully–Pythonic software to implement the 3DVAR framework for high–resolution three-dimensional wind retrievals. PyDDA was created to be open–source and function with no restriction on the number of radars and models that can be added to create a given retrieval(Jackson et al., 2020). PyDDA has been written fully in Python, using the standard packages such as NumPy (Harris et al., 2020), SciPy (Virtanen et al., 2020), Cartopy (Met Office, 2010 - 2015), and matplotlib (Hunter, 2007), along with the Python ARM Radar Toolkit (PyART) (Helmus and Collis, 2016).

1.6 Objectives and Contribution of Thesis

This work contributes to improving the near–surface characterization of the kinematics of thunderstorm downbursts. We utilize the similarity between impinging jet models and near-surface winds in downburst outflows to assess the retrieval of downburst winds. The base of this project is the Pythonic Direct Data Assimilation (PyDDA) framework, which assimilates data from an arbitrary number of radars to retrieve a high–resolution three–dimensional wind field (Jackson et al., 2020). However, the PyDDA has not been tested for its accuracy in retrieving downburst-like outflows. By utilizing idealized downburst-like impinging jet data with PyDDA, we attempt to improve the three-dimensional wind retrievals of thunderstorm downbursts. Assessing the PyDDA performances at retrieving these types of windstorm outflows is the first step toward improving our characterization of Doppler radar retrievals of downburst winds.

1.7 Organization of Thesis

The subsequent sections of the thesis are organized in the following manner:

Chapter 2 discusses the impinging jet model that was used to characterize downburst outflow near the surface. The parameters that are used in the model and the scaling of the small-scale impinging jet to a size of a typical downburst are described in Section 2.1.1. The radar functions for obtaining Doppler velocities in the idealized outflow from an arbitrary number of virtual radars are presented and tested in Section 2.1.2. The details of the Pythonic Direct Data Assimilation (PyDDA) framework and its use in Doppler retrieval are explained throughout Section 2.2.

Chapter 3 discusses the results of this research. The results are sorted into three groups: (1) presenting the PyDDA wind retrievals for a single Doppler radar (Section 3.1), (2) dual-Doppler radar retrievals (Section 3.2), and (3) dual-Doppler radars retrievals with missing low-level data (Section 3.3).

Chapter 4 provides the main conclusions of this research. This chapter also includes a summary of the work presented in Chapters 1–3 (Section 4.1) as well as recommendations for future work (Section 4.2).

Chapter 2

Methodology

2.1 Modelling Downbursts

2.1.1 Choosing a Model

For this project, a model that could be implemented into Python at the scale of a full–scale idealized downburst outflow was required. This could be most easily done with equations to model the properly scaled radial wall jet, as described in Poreh et al. (1967). The experiments in this paper were done on a small scale, with orifice diameters ranging from 1–3 inches and a flat aluminum plate with a radius of 69 inches. From the six runs of the experiment, the paper establishes that the maximum velocity, U_m, and the jet thickness, δ, can be described by the equations:

$$\frac{U_m b}{\sqrt{K}} = 1.32\left(\frac{r}{b}\right)^{-1.1} \quad \text{or} \quad \frac{U_m r}{\sqrt{K}} = 1.32\left(\frac{r}{b}\right)^{-0.1} \tag{2.1}$$

and

$$\frac{\delta}{b} = 0.098\left(\frac{r}{b}\right)^{0.9} \quad \text{or} \quad \frac{\delta}{r} = 0.098\left(\frac{r}{b}\right)^{-0.1}, \tag{2.2}$$

where b is the nozzle height, K is the kinematic momentum flux, and r is the radial distance from the axis of symmetry. The kinetic momentum flux, K, can be calculated assuming that the effective area of the jet due to contraction was 0.611 of the orifice area with the equation:

$$K = 0.153\pi D^2 U_0^2, \tag{2.3}$$

where D is the diameter of the orifice and U_0 is the exit velocity of the air from the orifice. These equations require a renormalization group to allow us to solve for u at a given location in the model. Recently, Moeini and Romanic (2022) demonstrated that

$$\frac{u_r - u_H}{U_m - u_H} = 2.269 \exp\left(-1.505\eta\right)\eta^{0.305}; \quad \eta \equiv \frac{z}{\delta} \tag{2.4}$$

could be considered as a universal renormalization group over a variety of flow conditions, including those of the work by Poreh et al. (1967). In Eq. 2.4, u_H represents the horizontal velocity of the crossflow in which the jet is embedded at $z = H$ and u_r is the radial velocity.

For this work, Eq. 2.4 can thus be simplified to

$$\frac{u_r - \cancelto{0}{u_H}}{U_m - \cancelto{0}{u_H}} = 2.269 \exp\left(-1.505\eta\right)\eta^{0.305}; \quad \eta \equiv \frac{z}{\delta} \tag{2.5}$$

yielding

$$u_r(r,z) = 2.269 U_m \exp\left(-1.505\frac{z}{\delta}\right)\left(\frac{z}{\delta}\right)^{0.305}, \tag{2.6}$$

which is used in conjunction with

$$U_m = \frac{1}{b}\sqrt{K} \cdot 1.32\left(\frac{r}{b}\right)^{-1.1} \tag{2.7}$$

and

$$\delta = b \cdot 0.098\left(\frac{r}{b}\right)^{0.9} \tag{2.8}$$

from Eq. 2.1 and Eq. 2.2.

With these put together, the equations must be scaled up to represent a full–sized idealized downburst outflow. This can be done using the principles of similitude, looking at the diameter of the orifice, D, the height of the orifice hole above the ground, b, and the exit velocity of the air coming out of the nozzle, U_0. In order to scale these up, values for a typical downburst outflow are required. In Table 1 of his paper, Hjelmfelt (1988) lists the characteristics measured for multiple downbursts over multiple events. He includes the averages of these values over the events measured, which are: a depth of 700 m, a downdraft diameter of 1.8 km, and a maximum vertical (descending) velocity of 12 m/s in the downdraft. Doswell (1994) reports that to a first approximation, the maximum gust of a downburst outflow is roughly equal to the maximum downdraft speed, which we also see in Hjelmfelt's schematic in Fig. 1.4. For this research, we are interested in looking at a more severe case than the reported average of 12 m/s by Hjelmfelt, and will look to some other examples of values used in the impinging jet models for downburst outflows. Following Mason et al. (2009), an orifice diameter of 1000 m will be taken and the height of the orifice will be solved for to ensure geometric similarity between the experiments by Poreh et al. (1967) and the model. Poreh et al. (1967) tested six different experiment configurations by considering various orifice diameters and exit jet velocities while maintaining the same orifice height. In order to be the most similar to the general geometry of a thunderstorm downburst, the geometry of run six will be used as it has the largest orifice diameter of 3 inches at the height of 2 feet.

For our model to have geometric similarity, the following should hold true:

$$\frac{D_{\text{Poreh}}}{b_{\text{Poreh}}} = \frac{D_{\text{model}}}{b_{\text{model}}}, \tag{2.9}$$

where D represents the diameter of the orifice and b is the orifice height. With three of the four variables known, we can solve for b_{model}:

$$\frac{0.0762\ [\text{m}]}{0.6096\ [\text{m}]} = \frac{1000\ [\text{m}]}{b_{\text{model}}} \Rightarrow b_{\text{model}} = 8000\ [\text{m}]. \tag{2.10}$$

Given the large difference between the original orifice and the model, this results in a geometric scale of about 1:13000. While this value of b_{model} is too high for downbursts in the real atmosphere, the present work focuses on the retrieval of downburst outflow structure, and the orifice height is not of particular importance. In the sixth experimental setup by Poreh et al. (1967), the exit jet velocity was 333 ft s^{-1}, which is equal to about 101 m s^{-1}, and is thus much higher than what would be typical for a thunderstorm downburst. A velocity scale of 1:1 therefore cannot be used, so a velocity scale of about 4:1 will be taken instead.

Implementing this into Python, the first results of the model scaled up to a 4 km radius can be seen. Figure 2.1 shows the x–component velocity of the model from two perspectives: the first, a horizontal slice taken at $z = 30$ m, and the second, a vertical slice taken at $y = 0$ m.

In both cases, we observe that the maximum x–velocity is around 30 m s^{-1}. With the exit velocity of the impinging jet being 25 m s^{-1}, the maximums hovering around 30 m s^{-1} are reasonable and follow Doswell (1994) findings that the maximum gust of a downburst outflow should be roughly equal to the maximum downdraft speed, to a first approximation. With

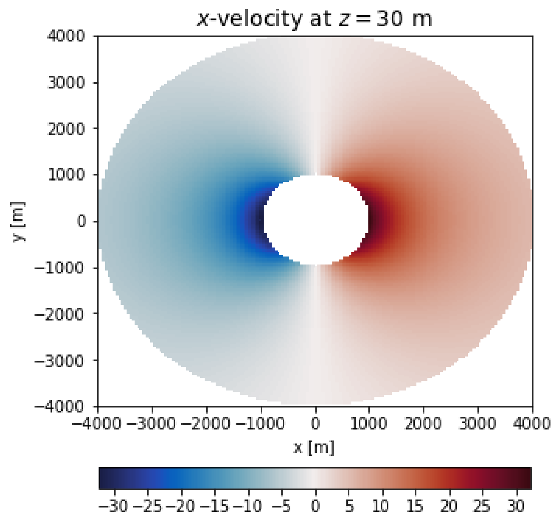

(a) Horizontal slice taken at $z = 30$ m.

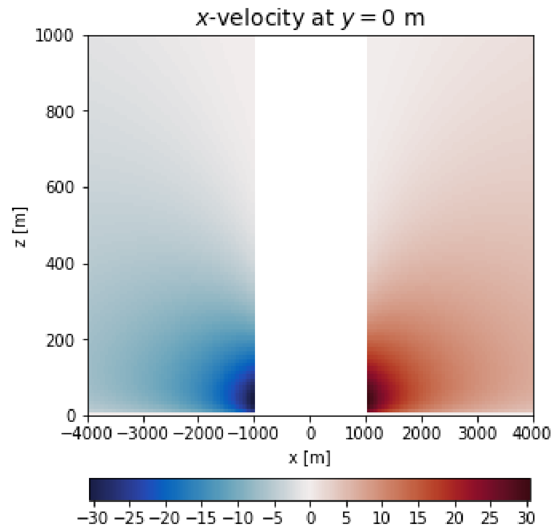

(b) Vertical slice taken at $y = 0$ m.

Figure 2.1: The x–component velocity of the model. The scaled–up orifice diameter is 1000 m and the exit–jet centreline velocity is 25 m s^{-1}. The white regions denote the areas of the model that are outside of the radial wall jet region (see Fig. 1.5).

both the x– and y–components of the velocity, it is now possible to use a virtual Doppler radar to extract radial velocities (also known as the line–of–sight velocities or Doppler velocities) and implement this model of idealized downburst outflow into the PyDDA framework.

2.1.2 Creating a Virtual Doppler Radar

In order to look at the model from the perspective of a virtual Doppler radar, a function calculating the velocity depicted by a virtual Doppler velocity radar at a given location in the flow field is required. Namely:

$$v_{\text{Doppler}}(z(r), \phi) = u(z)\cos\theta'\sin\phi + v(z)\cos\theta'\cos\phi + [w(z) - w_f]\sin\theta', \tag{2.11}$$

where z is the height, r is the radial distance from the radar along the beam, ϕ is the azimuth angle, θ' is the elevation of the radar beam, (u, v, w) are the three-dimensional Cartesian components of the wind, and w_f is the fall speed of the targets with respect to air (Fabry, 2015). In the model created by Poreh et al. (1967), there is no vertical component of the velocity. Further, since the microphysics are not taken into account both $w(z)$ and w_f are zero, and thus Eq. 2.12 becomes:

$$v_{\text{Doppler}}(z(r), \phi) = u(z)\cos\theta'\sin\phi + v(z)\cos\theta'\cos\phi. \tag{2.12}$$

This equation for the Doppler velocity will be used throughout the following examples in this section, as well as in the results.

To ensure that the Doppler velocity equation is implemented correctly into the model, some examples from the NOAA's (2007) "Guide For Interpreting Doppler Velocity Patterns" were recreated. These examples give the wind profile with graphs of both the wind direction and speed as a function of height, making them easy to recreate. Figure 2.2 shows the first and most simple example of a constant wind field. Further examples of more complicated wind fields were also completed and are available in Appendix A.

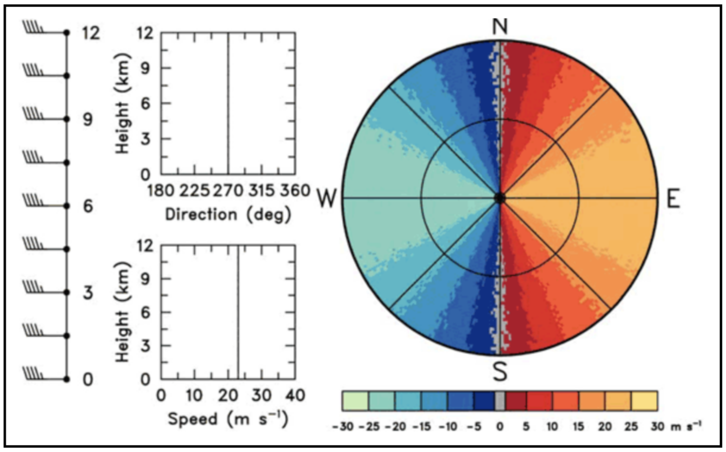

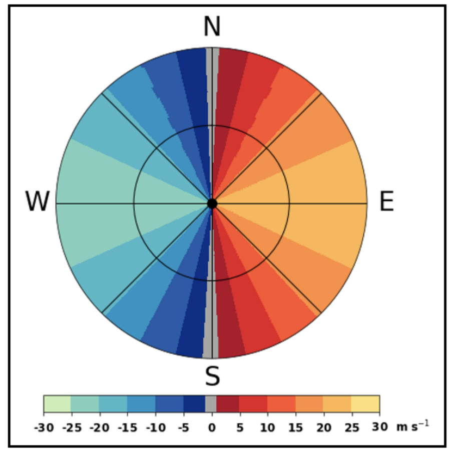

Figure 2.2: (**Left**) Doppler velocity pattern corresponding to a vertical wind profile where both speed (23 m s^{-1} or 45 kt) and direction (270°) are constant with height. Negative (positive) Doppler velocities represent flow toward (away from) radar. Radar is at the centre of the display. Caption and Figure taken from (NOAA, 2007). (**Right**) Recreation of this wind field using a Python model developed for this study.

Using the virtual Doppler radar function, the impinging jet model discussed can be assessed from the perspective of a single radar at a given location before it is implemented into PyDDA. The horizontal resolution of the data taken is 50 m and the vertical resolution is 10 m. This resolution was found to provide sufficient detail in the data without leading to long run times of the code or the kernel dying.

Four different radar locations were selected: one in the centre of the outflow, one 10 km south of the centre of the model (i.e., the centre of the downburst outflow), one 10 km east of the centre of the model, and one 20 km east of the centre of the model. Figure 2.3 shows the cases of a Doppler radar placed 10 km to the east of the centre of the outflow (Fig. 2.3a), a Doppler radar placed at the centre of the outflow (Fig. 2.3b), and a Doppler radar placed 20

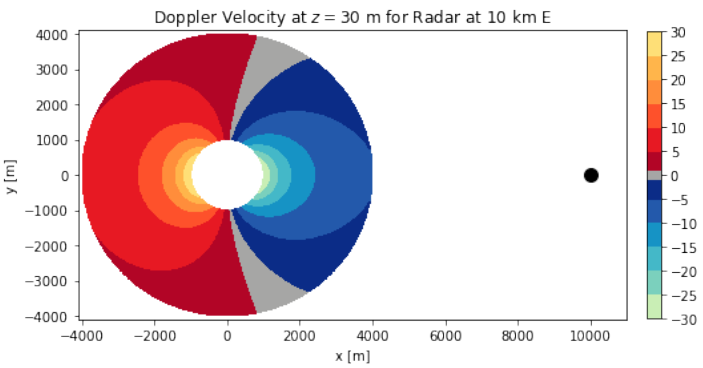

(a) The model as depicted by a radar located 10 km to the east of the centre of the model.

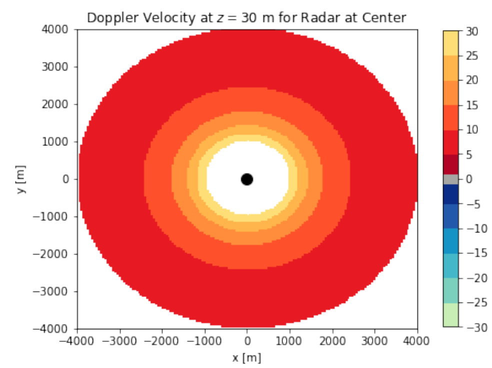

(b) The model as depicted by a radar located at the centre of the model.

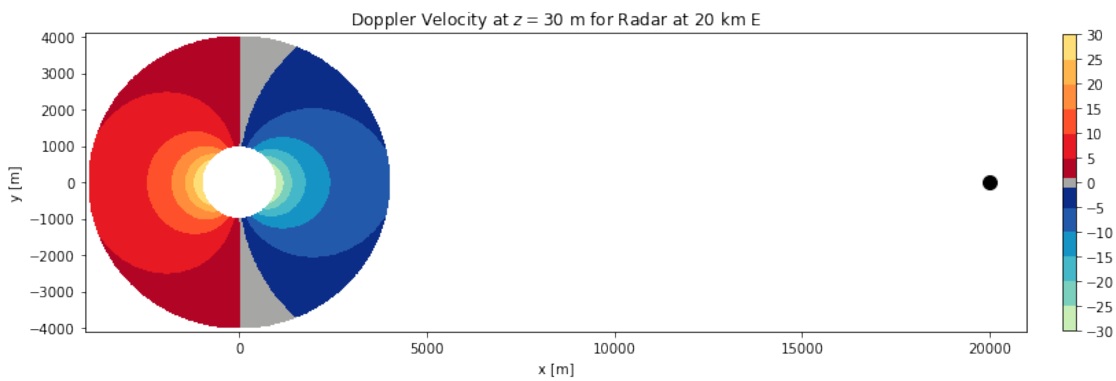

(c) The model as depicted by a radar located 20 km to the east of the centre of the model.

Figure 2.3: Doppler velocity of the model for three radars in different locations. The radar position in relation to the model downburst outflow is marked by a black dot. The white regions denote areas of the model that are outside of the radial wall jet region (see Fig. 1.5).

km to the east of the centre of the outflow (Fig. 2.3c). The case of a Doppler radar placed 10 km to the south of the centre of the outflow is the same but perpendicular to that placed 10 km to the east. The figure showing for this scenario can thus be found in Appendix A.2.

2.2 The Pythonic Direct Data Assimilation Framework

The Pythonic Direct Data Assimilation Framework (PyDDA) was developed in order to create a fully–Pythonic software that implemented the 3D variational (3DVAR) framework for three–dimensional wind retrievals using an arbitrary number of radar and model inputs. PyDDA is hosted and distributed on GitHub, allowing users to employ and edit it in an open–source fashion (`https://github.com/openradar/PyDDA`).

2.2.1 Use of a Vertical Vorticity Equation

The foundation of the work in this thesis is to improve the wind retrievals of thunderstorm downbursts is the lack of data close to the surface. Therefore, exploring options to improve this modelling further will help us to enhance this work. Shapiro et al. (2009) investigated the use of a vertical vorticity equation in variational dual–Doppler wind analysis, measuring the value added by it in the scenario of missing low–level data. Specifically, they withheld any data in the layer between the surface and 1.5 km in altitude. This work was used to help build PyDDA, and is thus foundational in its function.

Their analysis was done using a three–dimensional Beltrami flow, in particular, the one used by Shapiro (1993), sampled by two virtual Doppler radars. In general, Beltrami flows are exact solutions of the Navier-Stokes equations in which the vorticity field is aligned with the velocity field, such that

$$\boldsymbol{\omega} \times \mathbf{v} = 0. \tag{2.13}$$

By using this we are assuming that the flow satisfies the impermeability condition at the surface so that $w = 0$, but does not satisfy the free–slip or no–slip boundary conditions. Since these analyses neglected any low–level data, the largest convergence or divergence signatures did not enter the analysis. This approach is similar to the objectives of this work and the results from this paper could be extended to look at downbursts specifically in the manner that we have discussed. The authors noted that the experiments done do emulate flows such as at the base of a convective storm updraft, at the leading edge of a density current, in the lower part of a microburst, or in the rear flank downdraft of a supercell (Shapiro et al., 2009).

The best results of these analyses were seen when both the impermeability condition and the vorticity constraint were imposed, and when the radar scan periods were small. For larger scan periods, the benefits of this analysis were diminished, though there was still a noted improvement compared to the analysis without the vorticity constraint.

2.2.2 The 3DVAR Framework

The basis of the PyDDA is its use of the 3DVAR framework. It minimizes a sum of cost functions that are related to the given radar measurements, as well as equations of motion, balloon profiles of wind measurements, and forecasting models, to name a few constraints.

This technique has been shown to produce better wind retrievals near the top of storms than traditional methods, and has also shown a smaller but still significant improvement of wind retrievals near the ground (Potvin et al., 2012a; Gao et al., 1999a). The three traditional methods that the 3DVAR framework is compared to in Potvin et al. (2012a) were performed using the Custom Editing and Display of Reduced Information in Cartesian space (CEDRIC; Miller and Fredrick, 1998) software. In the traditional methods, the initial estimations of the analysis wind components u^a and v^a were obtained using the equations for u and v taken from Ray et al. (1980):

$$u = \frac{R_1V_1(y-y_2) - R_2 - V_2(y-y_1)w_f[(z-z_1)(y-y_2)-(z-z_2)(y-y_1)]}{(x-x_1)(y-y_2)-(x-x_2)(y-y_1)} \\ - w\frac{[(z-z_1)(y-y_2)-(z-z_2)(y-y_1)]}{(x-x_1)(y-y_2)-(x-x_2)(y-y_1)} = C_1 - wC_2, \quad (2.14)$$

$$v = \frac{R_2V_2(x-x_1) - R_1V_1(x-x_2) - w_f[(z-z_2)(x-x_2)-(z-z_1)(x-x_2)]}{(x-x_2)(y-y_1)-(x-x_1)(y-y_2)} \\ - w\frac{[(z-z_2)(x-x_1)-(z-z_1)(x-x_2)]}{(x-x_2)(y-y_1)-(x-x_1)(y-y_2)} = C_3 - wC_4, \quad (2.15)$$

where V_1 and V_2 are the measured Doppler velocity values from two radars, (x_1, y_1, z_1) and (x_2, y_2, z_2) are the locations for each radar, (x, y, z) is a location on the grid, (u, v, W) where $W = w + w_f$ represent the particle motion in the (x, y, z) directions, and w_f is the particle's terminal velocity. The initial estimation of w^a is $w^a = 0$, which is subsequently estimated after each iterative step. The w^a value is updated by integration of the anelastic continuity equation in each data column from the horizontal divergence field, δ^a, which is computed from u^a and v^a. At each iteration, the u^a and v^a values are used to calculate the new w^a using the equations 2.14 and 2.15 from Ray et al. (1980) until w^a converges. This process is completed for each data point in the field that is initially provided to PyDDA. Thus, the wind retrieval solution has the same horizontal and vertical resolution as the initial data.

If we let $\mathbf{v}(x,y,z) = (u(x,y,z), v(x,y,z), w(x,y,z)) \in \Re^3$ be the analysis wind field over a Cartesian grid, then it follows that $\mathbf{v}(x,y,z)$ is defined over a discrete Cartesian grid of (m,n,o) points as long as $(x_{ijk}, y_{ijk}, z_{ijk})$ for $i \in [0,m)$, $j \in [0,n)$, and $k \in [0,o)$. PyDDA determines the $\mathbf{v}(x_{ijk}, y_{ijk}, z_{ijk})$ for $i \in [0,m)$, $j \in [0,n)$ by identifying the $\mathbf{v}(x_{ijk}, y_{ijk}, z_{ijk})$ that minimizes the cost function:

$$J(\mathbf{v}) = C_O J_O + C_{\text{mass}} J_{\text{mass}} + C_V J_V + C_r J_r + C_S J_S + C_{\text{model}} J_{\text{model}} + C_{\text{point}} J_{\text{point}}, \tag{2.16}$$

where the C_n terms are the adjustable weighting coefficients for each constraint and the J_n terms are the cost functions. Each variable in Eq. 2.16 has its associated routine in PyDDA as listed in Table 2.1, and the subscripts represent the contributions of the radar observations, mass continuity equation, vertical vorticity equation, rawinsonde data, smoothness, model data, and point observations, respectively, to the total cost function. Each individual cost function calculates the sum of the squared discrepancies for a given constraint. The minimization of these cost functions minimizes the overall error of the wind retrieval in order to find a solution wind retrieval that uses all the components weighted according to the input coefficients. The weighting coefficients are adjustable by the user, so any uncertainties in the input data can be accounted for by the user in the wind retrieval by adjusting the weight of an individual cost function. A similar equation of the gradient $\nabla J(\mathbf{v})$ also exists in PyDDA, where $\nabla J(\mathbf{v})$ is the sum of the gradients $C_n \nabla J_n(\mathbf{v})$ for each of the same terms shown in Eq. 2.16.

The reason for the advantage of using the 3DVAR technique over traditional methods lies in the occurrence of severe errors aloft using traditional retrieval techniques. These errors occur regardless of whether or not the continuity equation integration goes upward, downward, or in both directions. When using traditional methods, the upward integration of the anelastic continuity equation yields errors that compound vertically due to the atmosphere's decrease in density with height, but the 3DVAR technique avoids the explicit integration of the continuity equation (Potvin et al., 2012a). The use of the 3DVAR framework also has the added advantage of being easier to incorporate observations from extra sensors and models and also being less sensitive to initial and boundary conditions than traditional methods (Jackson et al., 2020).

In order to find the $\mathbf{v}(x_{ijk}, y_{ijk}, z_{ijk})$ that minimizes the cost function of Eq. 2.16, PyDDA employs the Limited Memory Broyden–Fletcher–Goldfarb–Shanno Bounded (L–BFGS–B) optimization technique via SciPy (Virtanen et al., 2020; Liu and Nocedal,

Cost Function	**Symbol**	**Routine**
Total	$J(\mathbf{v})$	`J_function`
Radar observations	J_o	`calculate_radial_vel_cost_function`
Mass continuity	J_{mass}	`calculate_mass_continuity`
Vertical vorticity	J_V	`calculate_vertical_vorticity_cost`
Rawinsonde	J_r	`calculate_background_cost`
Smoothness	J_s	`calculate_smoothness_cost`
Model	J_{model}	`calculate_model_cost`
Point observations	J_{point}	`calculate_point_cost`

Table 2.1: The list of cost functions that are currently implemented in PyDDA. Taken from Jackson et al. (2020).

1989). The retrieval module of PyDDA encompasses the 3DVAR technique using the L–BFGS–B optimization. Iterations of L–BFGS–B are run until convergence is reached, where convergence is defined to be when $|\nabla J(\mathbf{v})| < 10^{-3}$ or when the point with the maximum change in w across the wind field is less than 0.2 [m s^{-1}] over 10 iterations.

PyDDA provides an initialization module that standardizes the form of the initial $\mathbf{v}$ while also allowing for the user to add custom initializations. By using the matplotlib and cartopy libraries from Python, the PyDDA visualization module allows the user to plot wind barbs and streamlines over gridded radar reflectivity fields.

2.2.3 Examples of PyDDA's Applications

With the open–source material on the PyDDA Github, multiple examples of how to use and run the software are given with the accompanying data to allow users to run the examples themselves. The most relevant of these examples to our work is the "Example on retrieving and plotting winds" by Robert C. Jackson. This is a simple example of how to retrieve and plot winds from 2 radars using PyDDA, which can also be edited to learn more about all of the functions that PyDDA provides. The data from this example is not relevant to our research, but the tools and functions that are implemented into PyDDA will be used and examined later in the thesis.

After reading in the radar data, the example starts with using the initialization module to create the initial wind field. The initial wind is set to a constant wind field of 0, which will be used later in our research as well. Apart from a constant wind field, the initialization modules include functions to make a 3D wind field from a sounding, make an initialization field based on the u and w from a numerical model run (e.g., Weather Research and Forecasting model), and read reanalysis data (e.g., ERA Interim) in NetCDF format and add it to a Py–ART Grid object. Py–ART's Grid is a class made for storing rectilinear gridded radar data in Cartesian coordinates and is what PyDDA uses to keep all data in one standard format.

Since all of the processes of PyDDA are already coded into functions, the next step in the example is to derive the final wind field. Using the "get_dd_wind_field" function in the retrieval module we can input the weighting of all of the adjustable weighting coefficients as defined by Eq. 2.16. In this example, only the mass continuity (C_{mass}) and observed radial velocities (C_O) are given weight, which are $C_{\text{mass}} = 256.0$ [m^2 s/kg] and $C_O = 1.0$ [s^2/m^2]. All other coefficients, for the smoothness in the x, y, and z directions, and the vertical vorticity equation are set to 0.0 in this example. The fall speed is calculated using the methodology of Biggerstaff and Betten in Potvin et al. (2012a), which uses the reflectivity and freezing level values to calculate fall speed. Their work uses the $w_f - Z^{obs}$ relation from Joss and Waldvogel (1970). In this example, the freezing level is set to 5000.0 [m]. After the first pass of iterations of the retrieval, the data is put through a low pass filter. The Savitzky-Golay filter function, savgol_filter, from SciPy's signal processing package is used (Virtanen et al., 2020). The filter window size can be adjusted when the function is run, where a larger value of the window size increases the smoothness and a smaller value would reduce it. The window size for the low pass filter is automatically set to 5, and will not be changed for this example. The upper boundary impermeability condition is also set, making $w = 0$ at the top of the atmosphere. There are many other parameter options when using the "get_dd_wind_field" function, which can be explored as further tests are done using PyDDA.

By running these parameters in PyDDA the 3D wind field is created and can be plotted. Using the capabilities of the PyDDA visualization module, we can look at the wind field from different levels and planes. Looking at the lowest altitude available to us in this example (1.05 km) from the x–y plane, we get the visualization shown in Figure 2.4. This plot uses barbs to show the horizontal cross–section of winds, though other options are available through the visualization module including streamlines or quivers. In this plot, the wind bards have been masked to show only inside of the two circles around the radars. These circles indicate where the PyDDA wind retrieval is most reliable. Taking a look at the x–z plane, we can see the wind field for all altitudes along a selected location of the plane. Figure 2.5 shows two

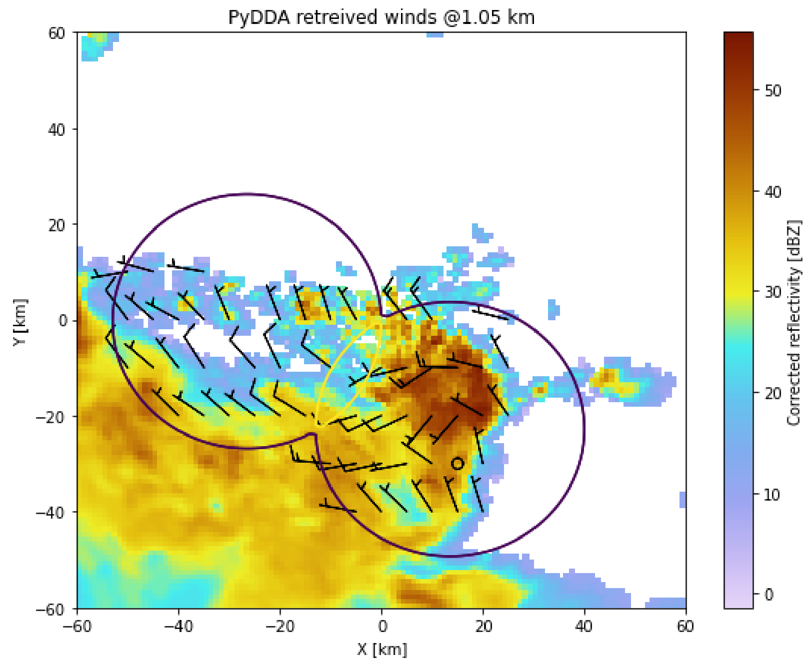

Figure 2.4: The wind field of the x–y plane taken at the first available level of 1.05 km in altitude. The wind field is represented by wind barbs set 5 km apart in the x–direction and 10 km apart in the y–direction. The two circles indicate the area where the PyDDA wind retrieval is most reliable.

examples of the same plot, with (a) showing the wind field represented by wind barbs and (b) using streamlines. The density of streamlines is not changed by the user like the amount of wind barbs, as it varies with the horizontal wind speed. Other visualization function options include the choice to add a geographical map, and each function has many parameters that can be changed to customize the look of the plots that are produced. In this example, the field of the y–z plane was also produced, but to conserve space we shall not include the plot here as it is done similarly to the x–z plane.

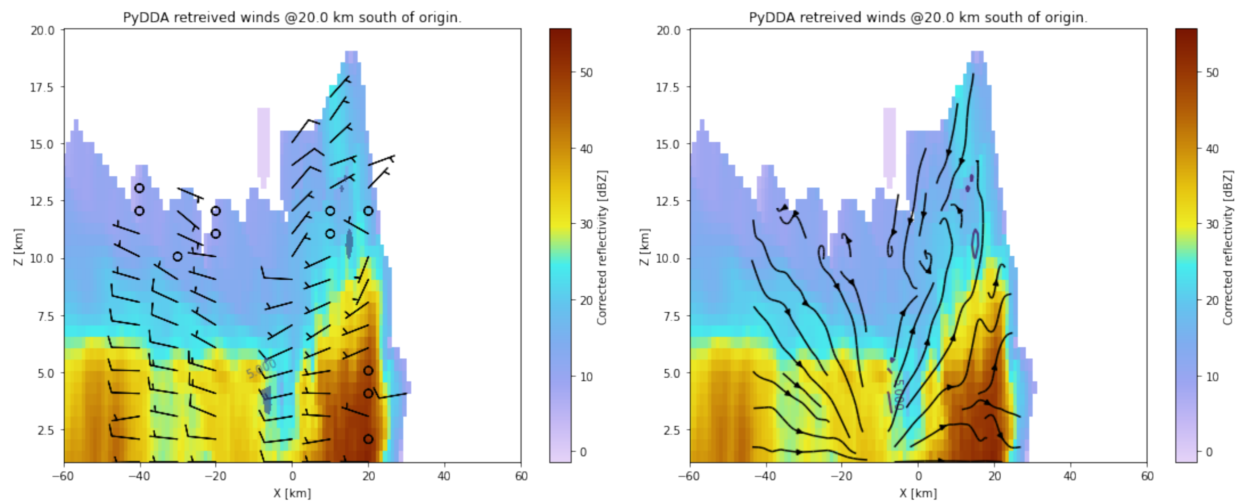

(a) The wind field represented with wind barbs. **(b)** The wind field represented with streamlines.

Figure 2.5: The wind field of the x–z plane taken 20km south of the origin, showing two of the plotting features that are available in the PyDDA visualization module.

Chapter 3

Results and Discussion

3.1 PyDDA Retrieval for Full Wind Field

The full wind fields for each of the virtual Doppler radars observing the model will be put into PyDDA. However, there are some constraints and values required by PyDDA's wind retrieval function. In order to run, PyDDA requires not only the Doppler velocity field but also the reflectivity. Since this is virtual data, there is no corresponding reflectivity field. This data is taken and used to calculate the hydrometeor fall speed, following the methodology of Biggerstaff and Betten in Potvin et al. (2012a). Since the model of Poreh et al. (1967) is not considering any precipitation or microphysics, the value of the reflectivity can be set to -20 dBZ which will result in a negligible fall speed calculated by PyDDA.

The weighting of the different coefficients is also required for PyDDA to run a wind retrieval. If not otherwise specified, the default values set by PyDDA are as follows: C_o, the weighting coefficient for the data constraint is 1.0 [s^2/m^2], C_m, the weighting coefficient for mass continuity constraint is 1500.0 [m^2 s/kg], and **frz**, the freezing level used for fall speed calculation in meters is 4500.0. All other weighting coefficients are automatically set to 0. Since the data we are using is idealized, the mass continuity constraint does not need to be weighted so heavily in relation to the data constraint. Therefore, the starting values that we will specify to PyDDA will be 1.0 for both weighting coefficients. These will be discussed further in Section 3.3.1.

The last requirement to run the PyDDA retrieval with the model data is an initial wind field. PyDDA has a few different functions to create an initial wind field based on a constant wind field, from a vertical wind profile, from a WRF run, or from ERA Interim data. Since there is no background wind field in this model, and thus we are not taking into account a moving downburst, an initial wind field of zero is most appropriate. Using the PyDDA function to create a constant wind field, a wind field of zero is created for the entire domain.

All three individual virtual radars were tested. Figure 3.1 shows the example that was also shown in Fig. 2.3a. Examples of the other two radars, located at 20 km to the east and 10 km to the south of the centre of the model downburst outflow can be found in Appendix B.1. When each individual radar is provided to PyDDA independently, the solution is the line-of-sight velocity. This is likely caused by the cost function, which is minimized by compensating the horizontal divergence with the vertical convergence. If updating the

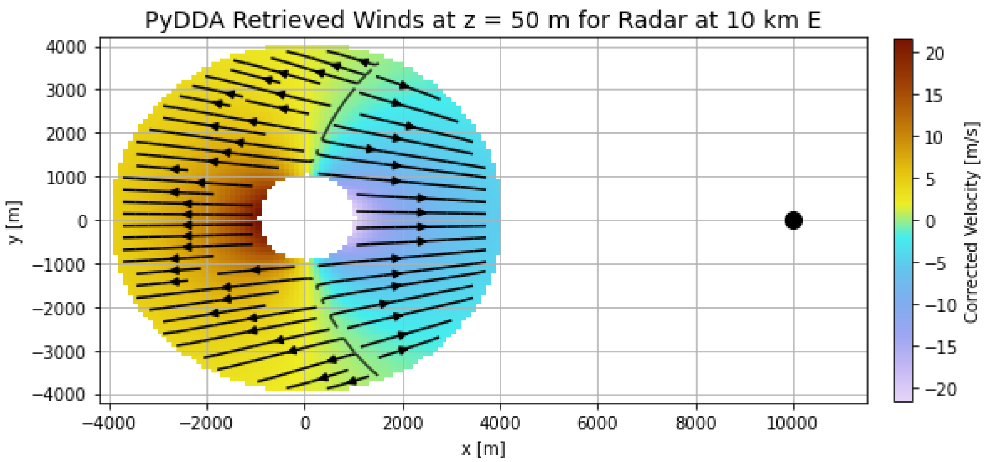

Figure 3.1: PyDDA retrieval for one radar located 10 km to the east of the centre of the model downburst outflow. The radar position in relation to the centre of the model downburst outflow are marked by black dots.

tangential component of the velocity does not lead to a reduction of $J(\mathbf{v})$ but updating the value of w does, then the algorithm pursues this approach to achieve minimization.

3.2 PyDDA Retrieval for Dual-Doppler Data

Multiple individual radars can be used in a PyDDA retrieval to improve the quality of the retrieval. Following the same process as was described in Section 3.1, the virtual radar data taken from 10 km to the south of the centre of the model downburst outflow can be combined in PyDDA with each of the radars located to the east.

Figure 3.2 shows the retrieval when two individual radars are used. A retrieval using the virtual radars 10 km to the south and 20 km to the east can be found in Appendix B.2. It

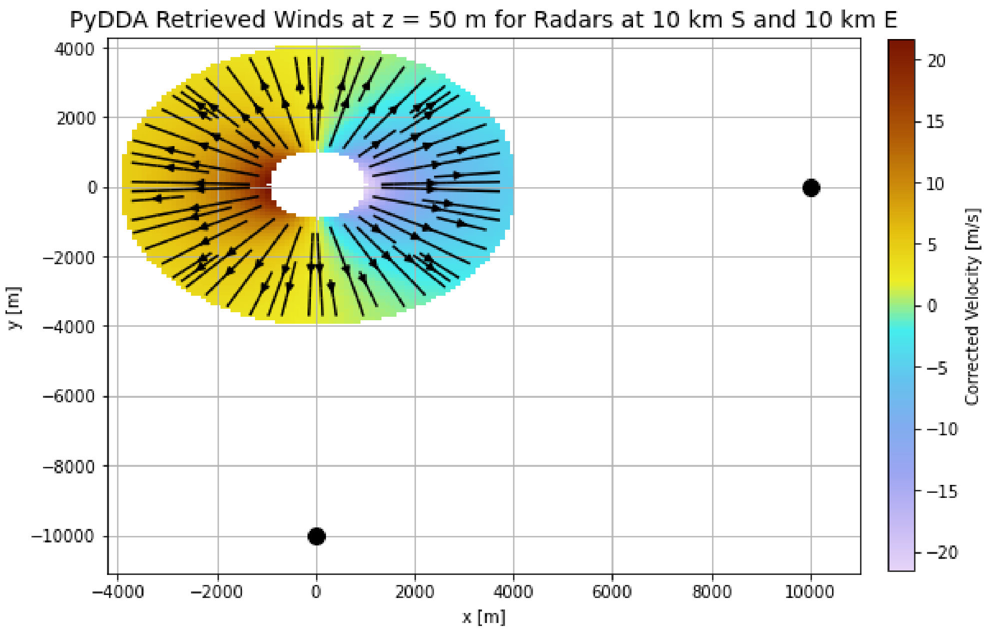

Figure 3.2: PyDDA retrieval for two radars, one 10 km to the south and 10 km to the east of the centre of the model downburst outflow. The radar positions in relation to the centre of the model downburst outflow are marked by black dots.

is clear how the Dual–Doppler data in Fig. 3.2 has improved the quality of the retrieval. Instead of seeing the model outflow from the perspective of a single Doppler radar as in Fig. 3.1, the full three–dimensional profile of the wind field can be seen.

3.3 PyDDA Retrieval for Missing Data

The same retrievals as discussed above will be recreated with the lowest 100 m of data withheld. This follows similarly to what was done by Potvin et al. (2012b).

3.3.1 Testing Weighting Coefficients

To ensure accuracy moving forward, the weighting coefficients should be perturbed to assess the sensitivity of the wind retrieval to different values of the coefficients. This will exemplify how the weight of the different constraints can affect the results of the retrieval. Retrieved wind fields using the values of the coefficients that are higher and lower than the default values are compared to the truth, which is the outflow modelled by the analytical expression developed by Poreh et al. (1967). This is done for both the weighting coefficient for the radar data, C_o, as well as for the weighting coefficient for the mass continuity equation, C_m.

Starting with the weighting coefficient for the mass continuity equation, the standard value of 1500.0 [m^2 s/kg] will be compared to the current value of 1.0 [m^2 s/kg] along with the value of 0.1 [m^2 s/kg] to look at a value less than 1.0 [m^2 s/kg]. Figure 3.3 shows the differences that these values cause when they are used. Figure 3.3 (a) shows that despite the changes in coefficient value, the PyDDA retrieved winds at 90 m maintain the same shape and are about a quarter of what they should be. Figure 3.3 (b) shows that for the standard value of C_m = 1500.0 [m^2 s/kg], the wind profile is further from the truth value than the values of C_m = 1.0 [m^2 s/kg] or C_m = 0.1 [m^2 s/kg]. All three retrievals with missing data have the same general shape, falling to zero at and below an altitude of 70 m above the surface.

These plots confirm that the value of the weighting coefficient C_m does not have a drastically negative impact on the results that have been seen thus far. The same test is

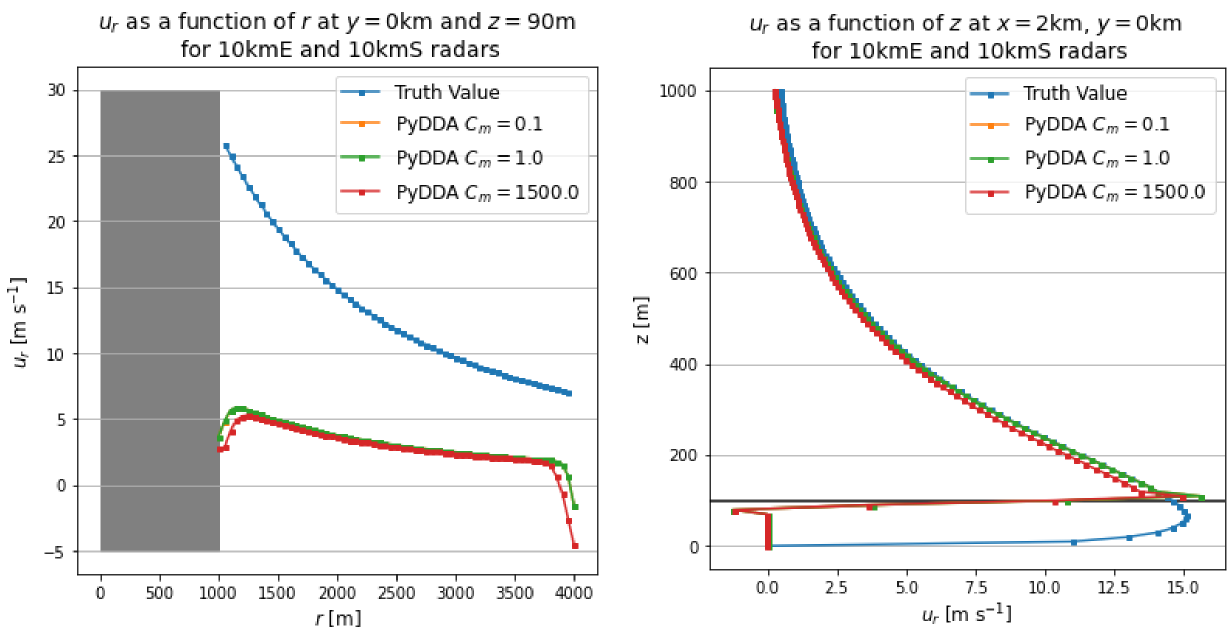

(a) **(b)**

Figure 3.3: The differences in wind profiles from the true value after being retrieved with PyDDA. **(a)** The wind velocity as a function of distance from the centre of the model at an altitude of 90 m above the surface. The grey region denotes the area in the centre of the model that is outside of the radial wall jet region (see Fig. 1.5). **(b)** The wind profile as a function of height for the location at $y = 0$ and $x = 2$ km. The horizontal black line denotes the 100 m altitude mark below which data is withheld.

now performed on the coefficient value for C_o, which will be changed to 0.1 [s^2/m^2] and 1500.0 [s^2/m^2] like for C_m.

Figure 3.4 shows the differences in the weighting coefficient for the radar data. The change between values is not as pronounced as it is when the value of C_m is changed. This shows that the value of 1.0 [m^2 s/kg] that has been used thus far is not negatively affecting the results that have been obtained.

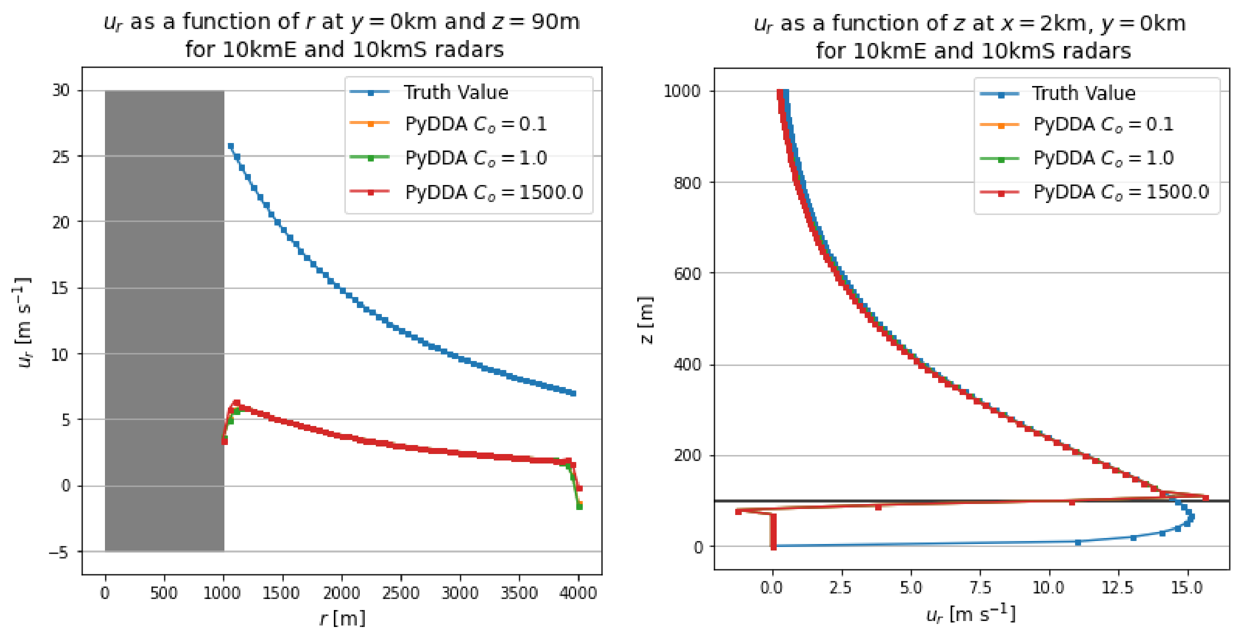

(a) **(b)**

Figure 3.4: The differences in wind profiles from the true value after being retrieved with PyDDA. **(a)** The wind velocity as a function of distance from the centre of the model at an altitude of 90 m above the surface. The grey region denotes the area in the centre of the model that is outside of the radial wall jet region (see Fig. 1.5). **(b)** The wind profile as a function of height for the location at $y = 0$ and $x = 2$ km. The horizontal black line denotes the 100 m altitude mark below which data is withheld.

In both Fig. 3.3 and 3.4, a very small increase in the mean error can be seen with increasing altitude. Although all retrievals have been set with reflectivity values such that the calculated fall speed is as small as possible, a very small value of w is calculated for each spacial point. This leads to a small underestimation of the u_r values as the altitude increases to compensate for the new w values that are not present in the model itself.

3.3.2 PyDDA Retrieval Performance with Initial Constraints

With the coefficient values confirmed, the profiles of the PyDDA retrieval can be looked at more closely. As seen in the previous section, the PyDDA retrievals obtain a differently shaped vertical wind profile than the nose-like profile that we expect to see. Figure 3.5 shows the vertical profile of two different locations at distances 1.5 km and 2.5 km from the centre of the model outflow. The truth value shows the nose-like profile in Fig. 1.5 that is expected using the model from Poreh et al. (1967). On the other hand, the PyDDA retrievals show some very different results near the surface. After following the truth profile closely from 1000 m down to 120 m in altitude, the PyDDA retrieval overshoots the velocity at 110 m in altitude before it undershoots at 100 m and 90 m, reaching a negative (converging) value at 80 m. After this, from 70 m to the surface, the value just becomes zero. This is the case for all locations that have been looked at anywhere within the model downburst outflow. Between the two vertical profiles in Fig. 3.5, we see the general shape is the same with a change in the maximum value at a radius of 1.5 km from the centre of about 22 m s^{-1} and at a radius of 2.5 km from the centre of about 12 m s^{-1}.

To look closer at the altitudes for which PyDDA performs poorly, Fig. 3.6 shows the horizontal wind profiles at an altitude of 90 m and 110 m. In Fig. 3.6 (a), we see that across the entire horizontal slice, the velocity shown by the PyDDA retrieval is roughly a quarter of the true value. The shape of the profile here is similar to that of the truth, with the exception of the ends closest to the outer limits of the model. This same shape towards the

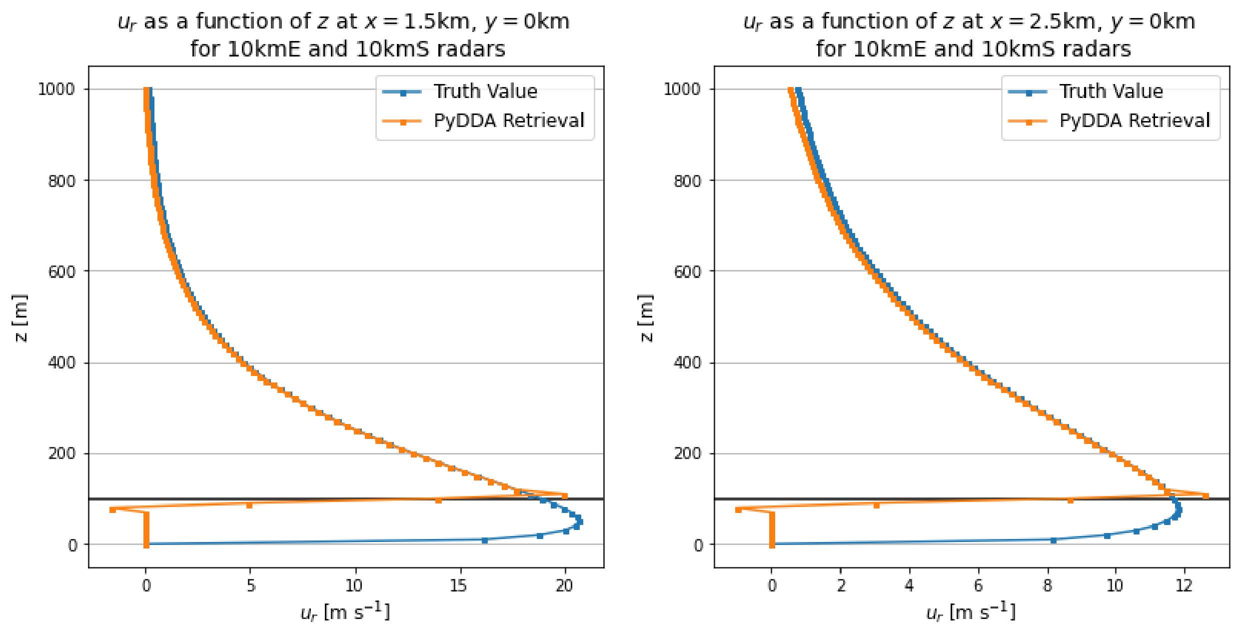

(a) The wind profile as a function of height for the location at $y = 0$ and $x = 1.5$ km.

(b) The wind profile as a function of height for the location at $y = 0$ and $x = 2.5$ km.

Figure 3.5: The differences in wind profiles from the true value after being retrieved with PyDDA.

outer edges of the model is also seen in Fig. 3.6 **(b)** at an altitude of 110 m. This is the only level where we see that PyDDA has overestimated the true value. Again, the general shape is similar here despite the slightly higher values.

Overall, when PyDDA is left to fill in gaps in the radar data given only the constraints for the data itself and the mass continuity equation, the results are poor. These constraints alone cannot fill in the near-surface data to any reasonable degree to help solve the problem of missing radar data.

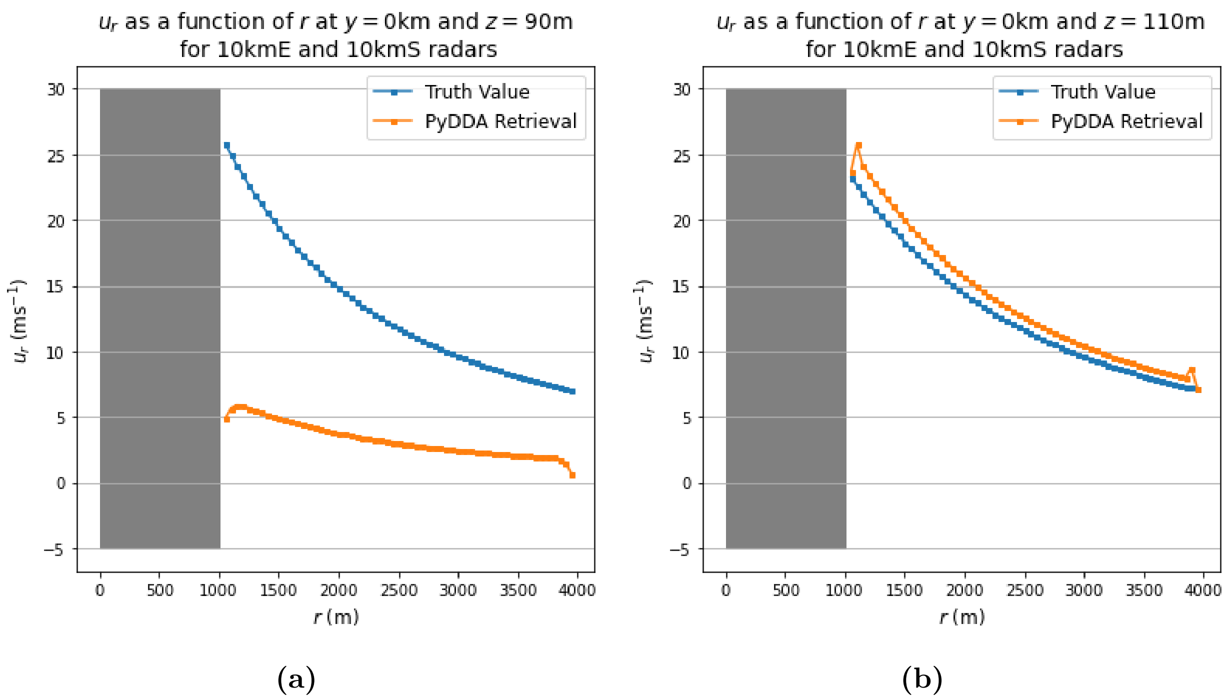

Figure 3.6: The differences in wind profiles from the true value after being retrieved with PyDDA. The horizontal black line denotes the 100 m altitude mark below which data is withheld. **(a)** The wind velocity as a function of distance from the centre of the model at an altitude of 90 m above the surface. **(b)** The wind velocity as a function of distance from the centre of the model at an altitude of 110 m above the surface.

3.3.3 Adding Further Constraints

One of the works cited by PyDDA in its development is the paper "Impact of a Vertical Vorticity Constraint in Variational Dual-Doppler Wind Analysis: Tests with Real and Simulated Supercell Data" by Potvin et al. (2012b). In this work, the 3DVAR framework is used in conjunction with the anelastic form of the vertical vorticity equation and constraints for the data, mass conservation equation, and smoothness. Their analysis was done on a larger scale (up to 6 km in altitude) than what has been done here and used a high-resolution ARPS supercell simulation instead of the impinging jet model we are looking at. They sought to improve the retrieval of the vertical component of the wind in the case of missing low–level data, removing data at an altitude of 1.5 km and below.

Within PyDDA, the vertical vorticity constraint depends on the given storm motion to be calculated. As there is no storm motion for our model, this makes the vertical vorticity constraint difficult to use. In the work by Potvin et al. (2012b), the smoothness constraints were also used for the $x-$, $y-$, and $z-$directions. This is possible to implement into our retrieval and could offer an improvement of the results shown in Fig. 3.5 and 3.6.

Figures 3.3 and 3.4 showed that the constraints for C_m and C_O are not particularly sensitive to perturbations of their values. Leaving these constraints at a value of 1.0, we can now look at the sensitivity of the wind retrieval to the different values of C_x, C_y, and C_z. Due to the nature of our diverging impinging jet model and the use of u_r to evaluate it, the coefficients for C_x and C_y will be tested together and the coefficient for C_z will be tested separately. In PyDDA, the initial values for C_x, C_y, and C_z are zero unless otherwise specified. Here, the same process as in Section 3.3.1 will be used to create three different wind retrievals with values of 0.1, 1.0, and 1500.0 to compare to the truth value of the model. All other constraints will be set to values of 1.0 unless otherwise specified.

Figure 3.7 shows the differences in the weighting coefficients for the smoothness in the $x-$ and $y-$directions. The values of C_z, C_O, and C_m are held constant at a value of 1.0. The

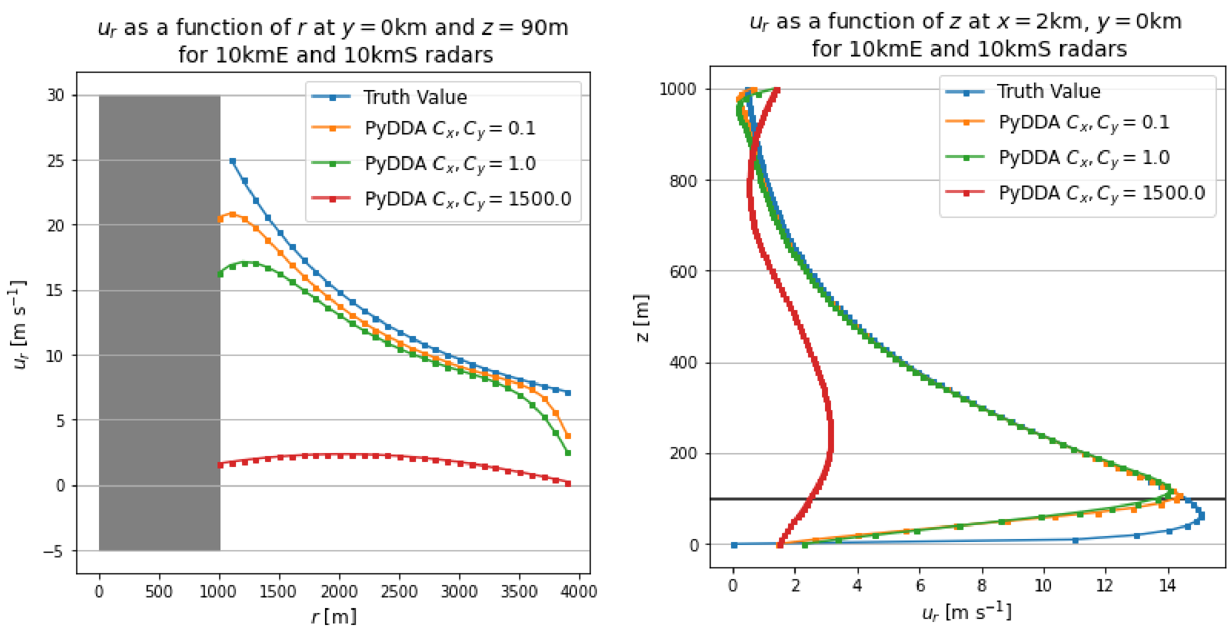

(a) **(b)**

Figure 3.7: The differences in wind profiles from the true value after being retrieved with PyDDA. **(a)** The wind velocity as a function of distance from the centre of the model at an altitude of 90 m above the surface. The grey region denotes the area in the centre of the model that is outside of the radial wall jet region (see Fig. 1.5). **(b)** The wind profile as a function of height for the location at $y = 0$ and $x = 2$ km. The horizontal black line denotes the 100 m altitude mark below which data is withheld.

change between values is much more pronounced than for C_O or C_m. Notably, the constraint values for 0.1 and 1.0 show a large improvement of the general shape of the wind profiles, especially below the data removal altitude of 100 m. There is a small difference between the two at the top of the profile as well as at the data cutoff altitude of 100 m. For the smaller value of C_x and C_y, the profile is slightly closer to the true values, though the overall shape of the profile is less smooth with its decrease in velocity to the surface. The constraint

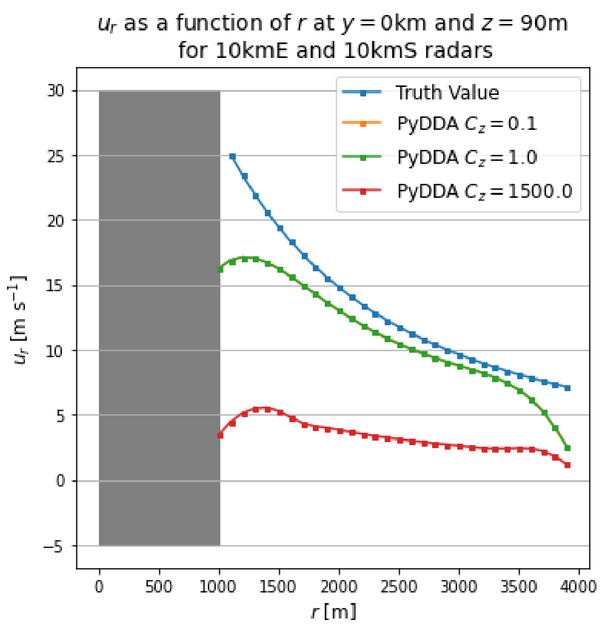

(a)

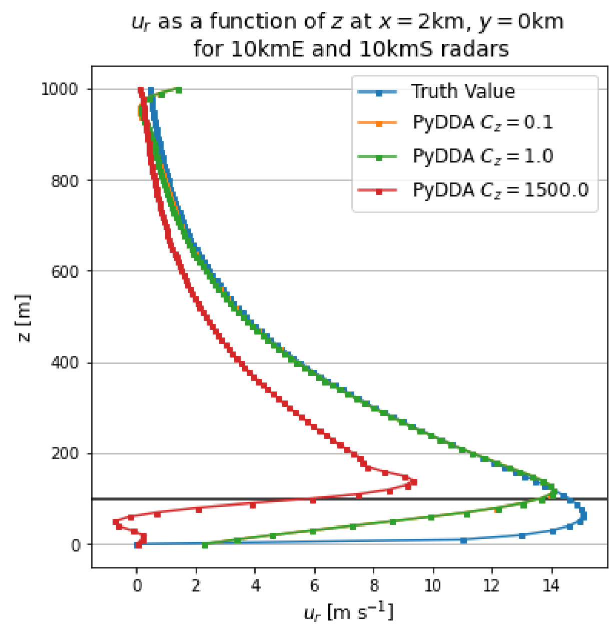

(b)

Figure 3.8: The differences in wind profiles from the true value after being retrieved with PyDDA. **(a)** The wind velocity as a function of distance from the centre of the model at an altitude of 90 m above the surface. The grey region denotes the area in the centre of the model that is outside of the radial wall jet region (see Fig. 1.5). **(b)** The wind profile as a function of height for the location at $y = 0$ and $x = 2$ km. The horizontal black line denotes the 100 m altitude mark below which data is withheld.

values of 1500.0 show a much larger sensitivity of the values than that of C_O or C_m, where such a high value of smoothing has changed the entire profile drastically at all altitudes. Apart from the improvements, we see that the smoothness constraints have also introduced more error at the very top of the vertical wind profile. It is also important to note how the retrieval below 100 m in altitude does not reach a value of zero for any altitude despite the perturbations. The radial wind u_r reaches a value of about 1.5 m s^{-1} at an altitude of 0 m, which is very different from the previous retrievals without the smoothness constraints which reached and maintained a u_r value of zero at and below about 70 m. Overall, the smoothness constraints in the $x-$ and $y-$ directions have a profound impact on the final wind retrieval and are much more sensitive to perturbations than either C_O or C_m.

Figure 3.8 shows the differences in the weighting coefficients for the $z-$direction. The values of C_x, C_y, C_O, and C_m are held at constant values of 1.0. The small change from a C_z value of 0.1 to 1.0 does not lead to a noticeable difference in the velocity profiles, however, the large change to 1500.0 does show an impact. The constraint for $z-$direction smoothness thus shows a larger sensitivity than that of C_O or C_m, but is less sensitive than C_x and C_y. The same trends seen in Fig. 3.7 can be seen here as well. The increase in error at the top of the velocity profile can be seen here with an improvement on the general shape for the value of $C_z = 1500.0$. However, for the same case, the shape of the velocity profile below the data cutoff altitude of 100 m takes a negative turn before reaching zero at the ground.

Both Fig. 3.7 and 3.8 show promising results of improvement over the previous profiles shown in Fig. 3.5 and 3.6. Use of the smoothness constraints along with those of the radar data and the mass coninuity equation can add value to the areas of missing data.

3.3.4 RMS Error of the Retrievals

In Potvin et al. (2012b), the results calculating the root mean square (RMS) error for the u– and v–components of the wind yielded error values of almost 16 m s^{-1} (for u–components) and 11 m s^{-1} (for v–components). The profiles of the RMS error for the u– and v–components of the wind can be found in Fig. 3.9. Notably, the error in both the u– and v–components of the wind increases below an altitude of 1.5 km where data was withheld.

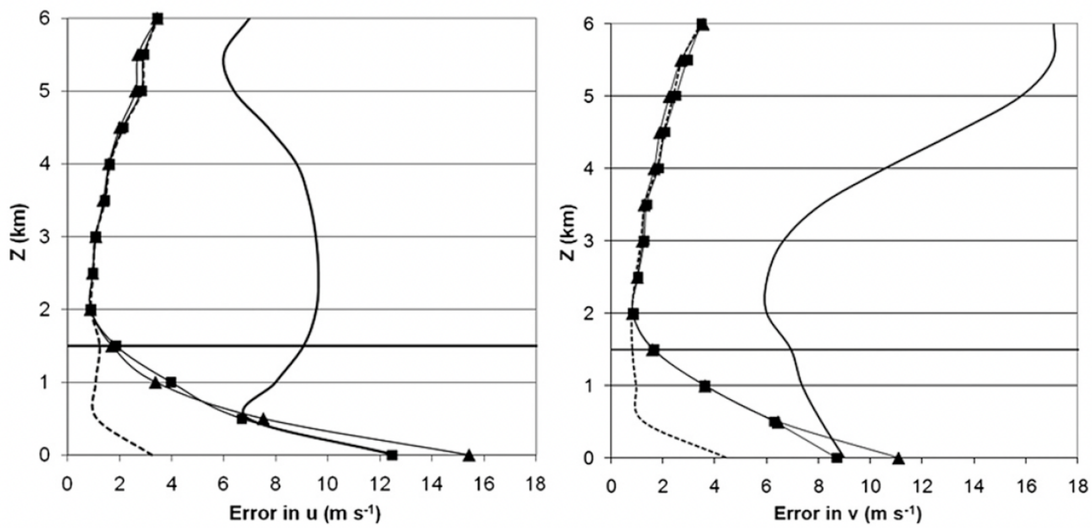

Figure 3.9: (left) The RMS error in the u–component wind. **(right)** The RMS error in the v–component wind. **(both)** The dashed lines represent the control values, the squares represent no use of the vertical vorticity equation, and the triangles represent the use of the vertical vorticity equation. The plain lines represent the true values of the u– and v–component winds. The bold horizontal line at 1.5 km in altitude represents the data cutoff height. Figure taken from Potvin et al. (2012b).

Reproducing this figure for the results of the downburst outflow model in PyDDA yields somewhat similar results, shown in Fig. 3.10. For this figure the radial velocity is shown instead of the u– and v–components of the wind because it is more meaningful for the diverging outflow of the model that was used.

In both the simulation done by Potvin et al. (2012b) and that done here, the error above

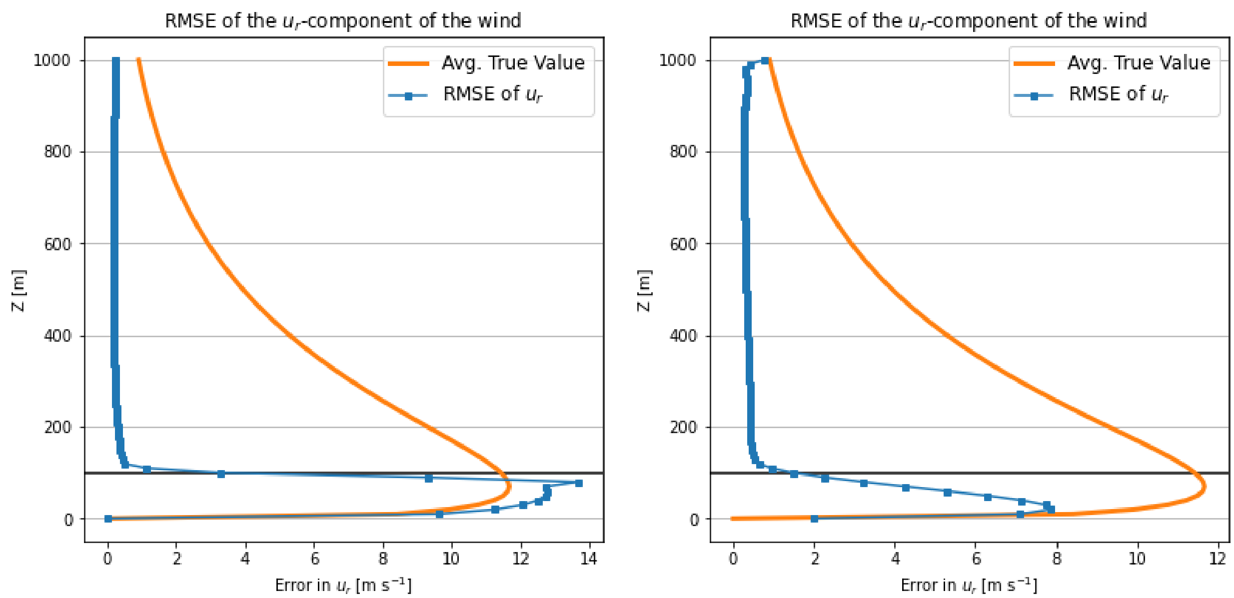

(a) **(b)**

Figure 3.10: The root mean square (RMS) error of the radial velocity (blue) and the average radial velocity value (orange) as a function of height. **(a)** For the retrieval using the C_O and C_m constraints. **(b)** For the retrieval using the C_O, C_m, C_x, C_y, and C_z constraints.

the data cutoff altitude is fairly small and may be primarily concentrated to the edges of the data. In both, the error here fluctuates slightly in proportion to the "true" value of the velocity, increasing when there is a higher average velocity and decreasing when it is lower. Below the cutoff altitude, the two figures have distinct profiles. In Fig. 3.9, the error increases with decreasing altitude from the data cutoff altitude of 1.5 km to obtain its highest error at the lowest level. For Fig. 3.10 **(a)** and **(b)**, the error peaks at the 80 m and 20 m levels, respectively. For Fig. 3.10 **(a)**, the error is lowest at the surface while in Fig. 3.10 **(b)** the error is lowest throughout the majority of data area. The cause of this difference between Fig. 3.9 and 3.10 is likely the result of the different velocity profiles between the two simulations. For the model downburst outflow, the average velocity at the surface is 0 m s^{-1}, with a peak velocity at about 60 m in altitude. The profile for the supercell simulation, however, does not go to zero at the surface and remains fairly constant for the v–component of the velocity and only varies by about 4 m s^{-1} for the u–component of the velocity.

PyDDA does use the 0 m s^{-1} velocity at the surface as one of its boundary conditions for the simulation only using the C_O and C_m constraints, which could be the reason that there is a large group of the lowest altitudes in Fig. 3.6 that have been set to 0 m s^{-1} in PyDDA's retrieval. Despite the different profiles between the two simulations, the RMS errors are very similar, maxing out at 14 to 16 m s^{-1}. In the case of the smoothness constraints, the boundary conditions of 0 m s^{-1} at the surface and the top of the simulation are not reached. Despite the higher error at these boundary altitudes, the error only peaks around 8 m s^{-1} at 20 m above the ground.

Unlike the high–resolution ARPS supercell simulation used by Potvin et al. (2012b), the model downburst outflow that was chosen for this project does not contain a w–component of the velocity. PyDDA does fill in and estimate the value of the w–component, and like the work done by Potvin et al. (2012b), we can assess the effects of the missing low–level data on the retrieval of these vertical component winds. Since the model has a w–component velocity of 0 m s^{-1} everywhere, any values of w in the final wind retrieval come from PyDDA itself. Figure 3.11 shows the difference in the w–component vertical profiles produced by the

PyDDA wind retrieval when PyDDA is provided with the full three–dimensional model wind field and the model wind field missing the lowest 100 m of data. The values that PyDDA retrieves for both profiles are very small, and ultimately are insignificant when compared to the values of the u– and v–components. Noticeably, when the smoothness constraints are added to the retrieval, the profile of the w–component velocity remains similar with and without the low-level data. This is not the case for the retrieval with only the C_O and C_m constraints, which is actually more similar below the 100 m cutoff altitude than it is above it.

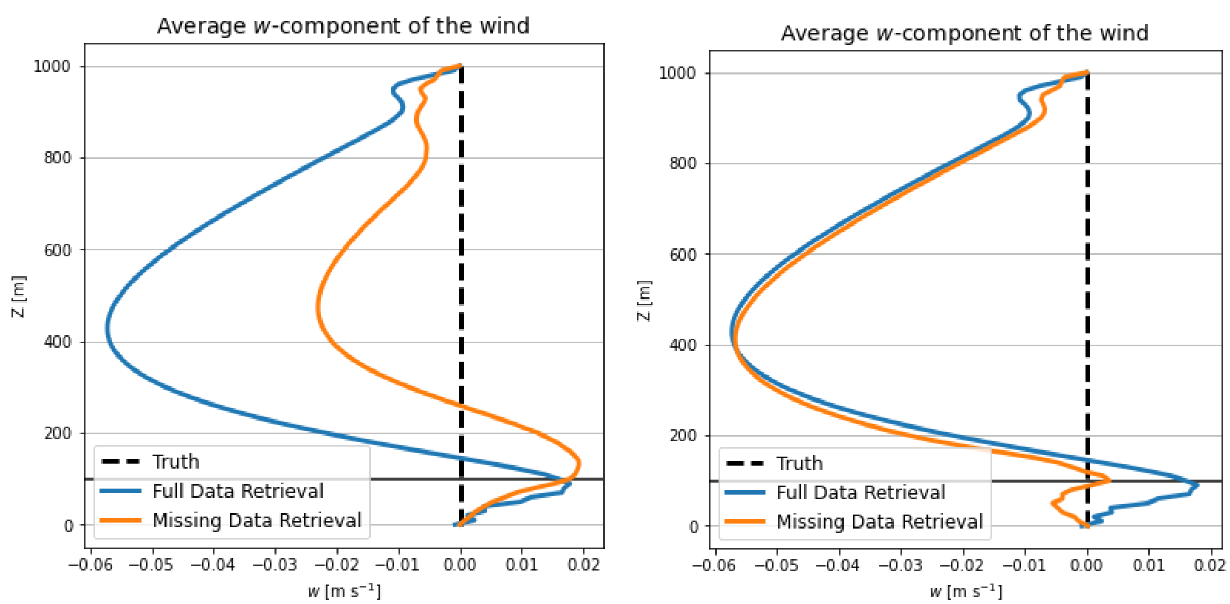

(a) **(b)**

Figure 3.11: The w–component of the velocity of two PyDDA wind retrievals, one produced with the full three–dimensional model wind field and the other produced with the wind field missing the lowest 100 m of data. **(a)** For the retrieval using the C_O and C_m constraints. **(b)** For the retrieval using the C_O, C_m, C_x, C_y, and C_z constraints.

Since there is no "truth" model value to compare to, we can only evaluate the effect that the missing data has on the profile when compared to the retrieval given the full model data. However, the difference in the two profiles when smoothness constraints are not considered shows a similar pattern to what is seen in Fig. 3.12.

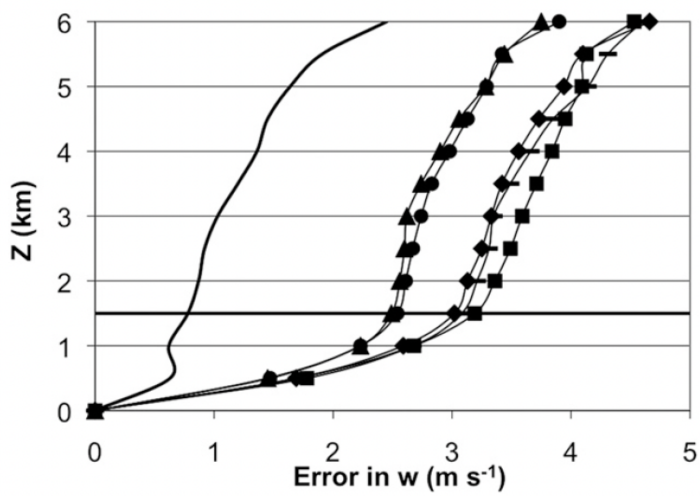

Figure 3.12: The RMS w^a errors in CONTROL (plain curve), NOVORT (squares), VORT (triangles), VORT-neither (diamonds), VORT-adv (circles), and VORT-direct (dashes) for $T = 2$ min. Figure and caption taken from Potvin et al. (2012b).

While the profiles themselves are not similar, the increase in error when there is missing low–level data affecting the entirety of the retrieval is. For the case of the model downburst outflow, we can use this information to improve the wind retrievals of downburst outflows with missing low–level data. Knowing the level of accuracy of the wind retrieval when it is produced with missing low–level data can be advantageous to those who depend on those results. By compensating for the error that is known to occur in the rest of the retrieval, we can improve the retrieval that is produced.

There are many constraints that PyDDA can take into account when creating a retrieval, all of which can be seen in Table 2.1. Of particular interest for these results is the option to use model data when producing a wind retrieval. Since this is an idealized case, the wind field that is given to PyDDA to create a retrieval is the model itself. In the case of real data, this model that has been used could be added as a model constraint to improve the quality of the final retrieval, especially if there is missing low–level data. The weighting coefficient of the model constraint could be adjusted such that it provides an appropriate amount of influence on the final retrieval. Any relevant analytical model could be used to create this constraint, not just that of Poreh et al. (1967) used in this research. Another analytical model that could be used is that of Vicroy (1991) based on the work of Oseguera and Bowles (1988). This is a simple, axisymmetric, steady–state analytical model of a microburst developed to estimate the vertical w–component winds from the horizontal wind measurements. It makes use of shaping functions to satisfy the mass continuity equation and to mimic the effects of the boundary layer (Vicroy, 1991). Further, it would be possible to move away from analytical models entirely and use experimental wind tunnel data as a constraint. With only the use of the dual–Doppler radar data and the mass continuity constraint, it is clear that the retrieval produced by PyDDA can use improvement.

As seen in the profiles of Fig. 3.5, PyDDA is not able to bridge the gap between the surface where the velocity is zero and the positive velocity it is given the constraints used in this exercise. At 80–100 m in altitude, there is a steep drop of the velocity of the PyDDA retrieval as it calculates a velocity that falls between its known value at 100 m and the zero it knows is at the surface. This retrieval could be improved with the model constraint allowing PyDDA to take into account the general vertical profile that the downburst outflow winds must follow so that it does not have such a steep decline to zero.

Chapter 4

Conclusions

4.1 Summary

The study of the phenomena of thunderstorm downbursts has come a long way since they were first identified with a name in 1977 (Fujita and Byers, 1977). The field campaigns NIMROD, JAWS, FLOWS, and MIST of 1978–86 produced much–needed data and facilitated the early study of micro– and macrobursts. As more has been learned about the structure and environments that facilitate their formation, forecasting and identifying them on dual–Doppler radar became possible. Learning more about their structure lead to the interest in modelling, which was originally done through two avenues: the modelling of the dynamics and thermodynamics of downbursts by scientists, and the simpler kinematic models for the use of flight simulators by the aircraft industry (Burlando and Romanic, 2021). This modelling has been facilitated by the creation of software used to generate three–dimensional wind retrievals such as CEDRIC and MultiDop.

In this work, the focus is the interaction of downburst outflows with the surface and their prediction in the case of missing low–level radar data. To facilitate this investigation, the analytical model of the radial wall jet presented by Poreh et al. is used (1967). These equations combined with the universal renormalization group presented by Moeini and Romanic (2022) allow us to create a three dimensional model of a downburst outflow for the u– and v–component winds.

PyDDA is a powerful tool for creating high–resolution three–dimensional wind retrievals in Python based on the 3DVAR framework. It can utilize data from numerous sources in its cost function including radar observations, mass continuity, vertical vorticity, rawinsonde, smoothness, model data, and point observations. For full three–dimensional wind fields with u– and v–components, PyDDA can estimate the value of the w–component.

In the case of missing low-level data, PyDDA can attempt to fill in data for the missing altitudes. When this is done only using the constraints for the dual–Doppler radar data and the mass continuity equation, the results have a high amount of error at the missing altitudes. This error is of the same order of magnitude as seen in the error for the work presented by Potvin et al. (2012b) for the u– and v–components of the retrieved wind field. When the smoothness constraints for the $x-$, $y-$, and $z-$directions are used with the constraints for the dual–Doppler radar data and the mass continuity equation, an improvement is seen with the data at the missing altitudes. This in turn reduces the error at these altitudes when compared to the original model data. It is possible that these results could be even further improved by using the model constraint in the cost function to give PyDDA a better baseline from which to calculate the retrieval. An analytical model such as the one used in this work by Poreh et al. (1967) or high-resolution experimental data from wind tunnel experiments could be implemented into the PyDDA cost function for use in the retrieval.

Thunderstorm downbursts are a severe weather phenomenon that will continue to occur and effect human activity. Although much has been learned about them in the past decades, the limitations in our current radar capabilities leave room for improvement. The ability to model the low–level data based on higher–altitude dual-Doppler radar data is advantageous to our overall knowledge of this phenomenon and our emergency preparedness. More work can be done in this area to allow for better interpretations of radar data, specifically when it comes to missing low–level data.

- For the case of a full three–dimensional wind field, PyDDA performs well and adds an estimation for the w–component of the wind.

- In the case of missing low–level data, namely below 100 m in altitude, PyDDA does not perform well in the estimation of the missing data and this affects its overall ability to estimate the w–component of the wind with the use of only the constraints for the dual–Doppler radar data and the mass continuity equation.

- The sensitivity of the weighting coefficients for the mass continuity equation and the radar data observations were not found to have a significant effect on these results.

- PyDDA's performance can be improved at and below the cutoff altitude with the addition of the smoothness constraints in the $x-$, $y-$, and $z-$directions. These constraints have a higher sensitivity of the weighting coefficient values than that of the mass continuity equation and the radar data observations.

4.2 Recommendations for Future Work

The results shown in Fig. 3.5 and 3.6 demonstrate the need for improvement of the wind retrievals produced by PyDDA for the case of missing low-level data. The addition of the smoothness constraints greatly reduces the error found at and below the cutoff altitude as seen in Fig. 3.10. Further improvement could be achieved by taking an analytical model, such as the one used throughout this work by Poreh et al. (1967) or that of Vicroy (1991), as a model constraint in PyDDA. Other types of models or experimental wind tunnel data could also be used for the model field. With a model constraint set to the appropriate weighting coefficient, PyDDA could use the velocity profiles of the model outflow to better find a solution when it is solving for missing data. As PyDDA is entirely open–source, a new constraint for this model could be created similar to the current model constraint used for numerical weather models. Another possible avenue of work is to implement the use of a time–dependent model, to use with a 4DVAR framework instead of the currently employed 3DVAR framework, which would be required to consider the transient nature of thunderstorm downbursts through their time dependency. This would require a different model than that of Poreh et al. (1967) so that the time dependent component of the thunderstorm downbursts could be considered.

Bibliography

Atkins, Nolan T. and Wakimoto, Roger M. (1991). “Wet Microburst Activity over the Southeastern United States: Implications for Forecasting”. In: *Weather and Forecasting* 6.4, pp. 470–482. DOI: 10.1175/1520-0434(1991)006<0470:WMAOTS>2.0.CO;2.

Bluestein, Howard B. (2013). *Severe Convective Storms and Tornadoes: Observations and Dynamics*. Berlin, Heidelberg: Springer. DOI: 10.1007/978-3-642-05381-8.

Bolek, Abdullah and Bayraktar, Seyfettin (2018). “Heat and fluid flow analyses of an impinging jet on a cubic body”. In: *Exergetic, Energetic and Environmental Dimensions*. Elsevier, pp. 677–693.

Burlando, Massimiliano and Romanic, Djordje (2021). “Chapter 4: Groundbreaking Contributions to Downburst Monitoring, Modeling, and Detection”. In: *The Oxford Handbook of Non-Synoptic Wind Storms*. Ed. by Horia Hangan and Ahsan Kareem. Oxford University Press. DOI: 10.1093/oxfordhb/9780190670252.013.10. URL: https://doi.org/10.1093/oxfordhb/9780190670252.013.10.

Byers, Horace Robert and Braham, Roscoe R. (1949). *The Thunderstorm: Report of the Thunderstorm Project*. U.S. Government Printing Office.

Doswell, CA (1994). "Extreme convective windstorms: current understanding and research". In: *Rep. of the Proceedings (1994) of the US-Spain Workshop on Natural Hazards (Barcelona, Spain, 8-11 June 1993), J. Corominas and KP Georgakakos, Eds*, pp. 44–55.

Fabry, Frédéric (2015). "Doppler velocity information". In: *Radar Meteorology: Principles and Practice*. Cambridge: Cambridge University Press, pp. 65–91.

Fujita, T. T. (1978). *Manual of downburst identification for Project NIMROD*. Tech. rep. NASA-CR-156953. URL: `https://ntrs.nasa.gov/citations/19780022828`.

Fujita, T. Theodore (1981). "Tornadoes and Downbursts in the Context of Generalized Planetary Scales". In: *Journal of the Atmospheric Sciences* 38.8, pp. 1511–1534. DOI: `10.1175/1520-0469(1981)038<1511:TADITC>2.0.CO;2`.

Fujita, T. Theodore and Byers, Horace R. (1977). "Spearhead Echo and Downburst in the Crash of an Airliner". In: *Monthly Weather Review* 105.2, pp. 129–146. DOI: `10.1175/1520-0493(1977)105<0129:SEADIT>2.0.CO;2`.

Fujita, T.T. (1985). *The downburst: microburst and macroburst ; report of projects NIMROD and JAWS*. SMRP research paper. University of Chicago, Department of the Geophysical Sciences.

Gal-Chen, Tzvi (1978). "A Method for the Initialization of the Anelastic Equations: Implications for Matching Models with Observations". In: *Monthly Weather Review* 106.5, pp. 587–606. DOI: https://doi.org/10.1175/1520-0493(1978)106<0587:AMFTIO>2.0.CO;2.

Gal-Chen, Tzvi and Kropfli, Robert A. (1984). "Buoyancy and Pressure Perturbations Derived from Dual-Doppler Radar Observations of the Planetary Boundary Layer: Applications for Matching Models with Observations". In: *Journal of Atmospheric Sciences* 41.20, pp. 3007–3020. DOI: https://doi.org/10.1175/1520-0469(1984)041<3007:BAPPDF>2.0.CO;2.

Gao, Jidong, Xue, Ming, Shapiro, Alan, and Droegemeier, Kelvin K (1999a). "A variational method for the analysis of three-dimensional wind fields from two Doppler radars". In: *Monthly weather review* 127.9, pp. 2128–2142.

— (1999b). "A Variational Method for the Analysis of Three-Dimensional Wind Fields from Two Doppler Radars". In: *Monthly Weather Review* 127.9, pp. 2128–2142. DOI: https://doi.org/10.1175/1520-0493(1999)127<2128:AVMFTA>2.0.CO;2.

Hadavi, Mohammad, Sun, Lutong, and Romanic, Djordje (2022). "Normalized insured losses caused by windstorms in Quebec and Ontario, Canada, in the period 2008–2021". In: *International Journal of Disaster Risk Reduction* 80, p. 103222.

Harris, Charles R., Millman, K. Jarrod, Walt, Stéfan J. van der, Gommers, Ralf, Virtanen, Pauli, Cournapeau, David, Wieser, Eric, Taylor, Julian, Berg, Sebastian, Smith, Nathaniel J., Kern, Robert, Picus, Matti, Hoyer, Stephan, Kerkwijk, Marten H. van, Brett, Matthew, Haldane, Allan, Río, Jaime Fernández del, Wiebe, Mark, Peterson, Pearu, Gérard-Marchant, Pierre, Sheppard, Kevin, Reddy, Tyler, Weckesser, Warren, Abbasi, Hameer, Gohlke, Christoph, and Oliphant, Travis E. (2020). "Array programming with NumPy". In: *Nature* 585.7825, pp. 357–362. DOI: 10.1038/s41586-020-2649-2.

Helmus, Jonathan J and Collis, Scott M (2016). "The Python ARM Radar Toolkit (Py-ART), a Library for Working with Weather Radar Data in the Python Programming Language". In: *Journal of Open Research Software*. DOI: 10.5334/jors.119.

Hjelmfelt, Mark R. (1988). "Structure and Life Cycle of Microburst Outflows Observed in Colorado". In: *Journal of Applied Meteorology and Climatology* 27.8, pp. 900–927. DOI: 10.1175/1520-0450(1988)027<0900:SALCOM>2.0.CO;2. (Visited on 05/26/2023).

Hunter, J. D. (2007). "Matplotlib: A 2D graphics environment". In: *Computing in Science & Engineering* 9.3, pp. 90–95. DOI: 10.1109/MCSE.2007.55.

Jackson, Robert, Collis, Scott, Lang, Timothy, Potvin, Corey, and Munson, Todd (2020). "PyDDA: A Pythonic Direct Data Assimilation Framework for Wind Retrievals". In: 8.1, p. 20. DOI: 10.5334/jors.264.

Joss, J and Waldvogel, A (1970). "Raindrop size distributions and Doppler velocity". In: *Preprints 14th Radar Meteor. Conf., Amer. Meteor. Soc.* Pp. 153–156.

Lang, T, Souto, M, Khobahi, S, and Jackson, B (2017). “nasa/MultiDop: MultiDop v0.3”. Version Version v0.3. In: DOI: https://doi.org/10.5281/zenodo.1035904.

Liu, Dong C and Nocedal, Jorge (1989). “On the limited memory BFGS method for large scale optimization”. In: *Mathematical programming* 45.1-3, pp. 503–528.

Mason, Matthew S., Wood, Graeme S., and Fletcher, David F. (2009). “Numerical simulation of downburst winds”. In: *Journal of Wind Engineering and Industrial Aerodynamics* 97.11, pp. 523–539. DOI: https://doi.org/10.1016/j.jweia.2009.07.010.

McCarthy, John, Wilson, James W., and Fujita, T. Theodore (1982). “The Joint Airport Weather Studies Project”. In: *Bulletin of the American Meteorological Society* 63.1, pp. 15–22. DOI: 10.1175/1520-0477(1982)063<0015:TJAWSP>2.0.CO;2.

Met Office (2010 - 2015). *Cartopy: a cartographic python library with a Matplotlib interface.* Exeter, Devon. URL: https://scitools.org.uk/cartopy.

Miller, L Jay and Fredrick, Sherrie M (1998). “Custom editing and display of reduced information in cartesian space (CEDRIC) manual”. In: *National Center for Atmospheric Research, Mesoscale and Microscale Meteorology Division, Boulder, CO.*

Moeini, Masoud and Romanic, Djordje (2022). “An Analytical Solution to The Perturbation Analysis of The Interaction between Downburst Outflows and Atmospheric Boundary Layer Winds”. In: *Journal of the Atmospheric Sciences.* DOI: 10.1175/JAS-D-22-0123.1.

NOAA, National Severe Storms Laboratory (2007). *A Guide for Interpreting Doppler Velocity Patterns*. URL: https://www.nssl.noaa.gov/publications/dopplerguide/.

Oseguera, Rosa M and Bowles, Roland L (1988). *A simple, analytic 3-dimensional downburst model based on boundary layer stagnation flow*. Tech. rep.

Poreh, M., Tsuei, Y. G., and Cermak, J. E. (1967). "Investigation of a Turbulent Radial Wall Jet". In: *Journal of Applied Mechanics* 34.2, pp. 457–463. DOI: 10.1115/1.3607705.

Potvin, Corey K., Betten, Daniel, Wicker, Louis J., Elmore, Kimberly L., and Biggerstaff, Michael I. (2012a). "3DVAR versus Traditional Dual-Doppler Wind Retrievals of a Simulated Supercell Thunderstorm". In: *Monthly Weather Review* 140.11, pp. 3487–3494. DOI: 10.1175/MWR-D-12-00063.1.

Potvin, Corey K., Shapiro, Alan, and Xue, Ming (2012b). "Impact of a Vertical Vorticity Constraint in Variational Dual-Doppler Wind Analysis: Tests with Real and Simulated Supercell Data". In: *Journal of Atmospheric and Oceanic Technology* 29.1, pp. 32–49. DOI: 10.1175/JTECH-D-11-00019.1.

Ray, Peter S, Ziegler, Conrad L, Bumgarner, William, and Serafin, Robert J (1980). "Single- and multiple-Doppler radar observations of tornadic storms". In: *Monthly Weather Review* 108.10, pp. 1607–1625.

Shapiro, Alan (1993). "The use of an exact solution of the Navier–Stokes equations in a validation test of a three-dimensional nonhydrostatic numerical model". In: *Monthly weather review* 121.8, pp. 2420–2425.

Shapiro, Alan, Potvin, Corey K., and Gao, Jidong (2009). "Use of a Vertical Vorticity Equation in Variational Dual-Doppler Wind Analysis". In: *Journal of Atmospheric and Oceanic Technology* 26.10, pp. 2089–2106. DOI: `10.1175/2009JTECHA1256.1`.

Vicroy, Dan D (1991). *A simple, analytical, axisymmetric microburst model for downdraft estimation*. Vol. 104053. National Aeronautics and Space Administration, Langley Research Center.

Virtanen, Pauli, Gommers, Ralf, Oliphant, Travis E., Haberland, Matt, Reddy, Tyler, Cournapeau, David, Burovski, Evgeni, Peterson, Pearu, Weckesser, Warren, Bright, Jonathan, van der Walt, Stéfan J., Brett, Matthew, Wilson, Joshua, Millman, K. Jarrod, Mayorov, Nikolay, Nelson, Andrew R. J., Jones, Eric, Kern, Robert, Larson, Eric, Carey, C J, Polat, İlhan, Feng, Yu, Moore, Eric W., VanderPlas, Jake, Laxalde, Denis, Perktold, Josef, Cimrman, Robert, Henriksen, Ian, Quintero, E. A., Harris, Charles R., Archibald, Anne M., Ribeiro, Antônio H., Pedregosa, Fabian, van Mulbregt, Paul, and SciPy 1.0 Contributors (2020). "SciPy 1.0: Fundamental Algorithms for Scientific Computing in Python". In: *Nature Methods* 17, pp. 261–272. DOI: `10.1038/s41592-019-0686-2`.

Wilson, James and Wakimoto, Roger (2001). "The Discovery of the Downburst: T. T. Fujita's Contribution". In: *Bulletin of the American Meteorological Society* 82. DOI: 10.1175/1520-0477(2001)082<0049:TDOTDT>2.3.CO;2.

Wilson, James W., Moore, James A., Foote, G. Brant, Martner, Brooks, Rodi, Alfred R., Uttal, Taneil, and Wilczak, James M. (1988). "Convection Initiation and Downburst Experiment (CINDE)". In: *Bulletin of the American Meteorological Society* 69.11, pp. 1328–1347. DOI: `https://doi.org/10.1175/1520-0477(1988)069<1328:CIADE>2.0.CO;2`.

Wolfson, M M, DiStefano, J T, and Forman, B E (1987). *The FLOWS (FAA-Lincoln Laboratory Operational Weather Studies) Automatic Weather Station Network in Operation*. Tech. rep. DOT-FAA-PM-85-27.

Wood, Graeme S, Kwok, Kenny CS, Motteram, Nicholas A, and Fletcher, David F (2001). "Physical and numerical modelling of thunderstorm downbursts". In: *Journal of Wind Engineering and Industrial Aerodynamics* 89.6, pp. 535–552.

Yao, Shiyong, Guo, Yong, Jiang, Nan, and Liu, Junjie (2015). "An experimental study of a turbulent jet impinging on a flat surface". In: *International Journal of Heat and Mass Transfer* 83, pp. 820–832.

Zhu, Shangxiang and Etkin, Bernard (1985). "Model of the wind field in a downburst". In: *Journal of Aircraft* 22.7, pp. 595–601. DOI: `10.2514/3.45171`.

Appendix A

Model Testing

A.1 Testing the Virtual Doppler Radar

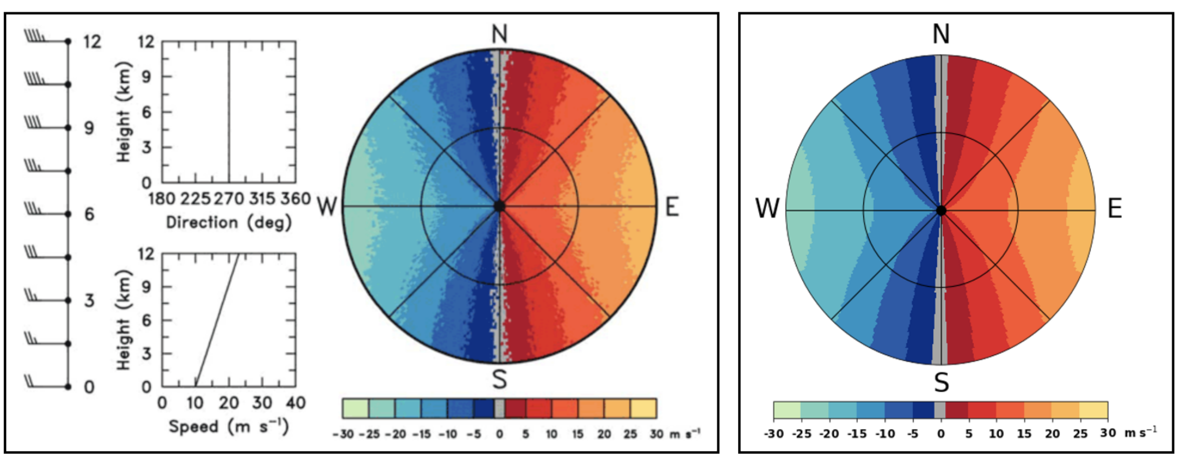

Figure A.1: (**Left**) Same as Fig. 2.2, except that the wind speed increases from 10 m s^{-1} (19 kt) at the ground to 23 m s^{-1} (45 kt) at the edge of the display. Caption and Figure taken from (NOAA, 2007). (**Right**) Recreation of this wind field using Python.

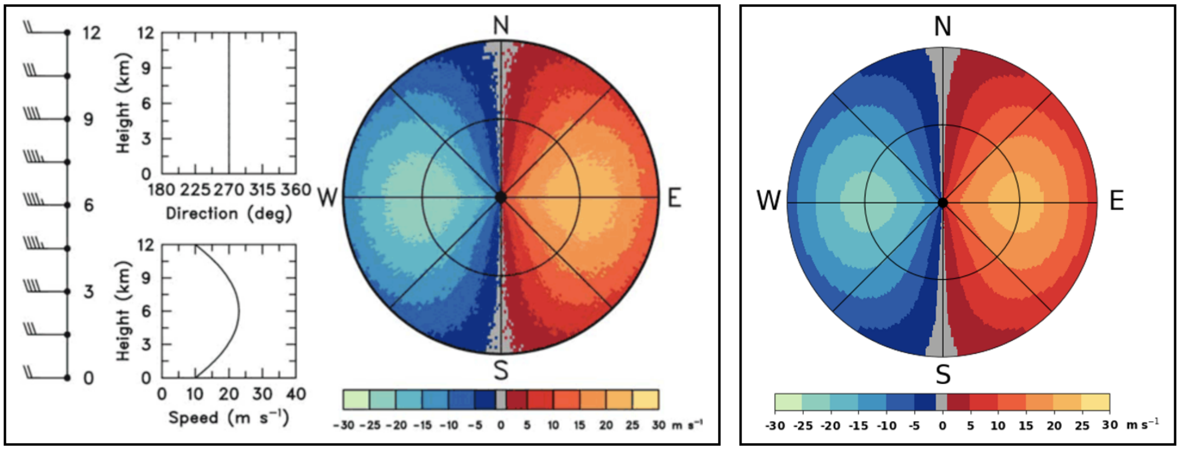

Figure A.2: (**Left**) Same as Fig. 2.2, except that the wind speed is a maximum of 23 m s^{-1} (45 kt) midway between the ground and the height corresponding to the edge of the display. Speed is 10 m s^{-1} (19 kt) at the surface and at the edge of the display. Caption and Figure taken from (NOAA, 2007). (**Right**) Recreation of this wind field using Python.

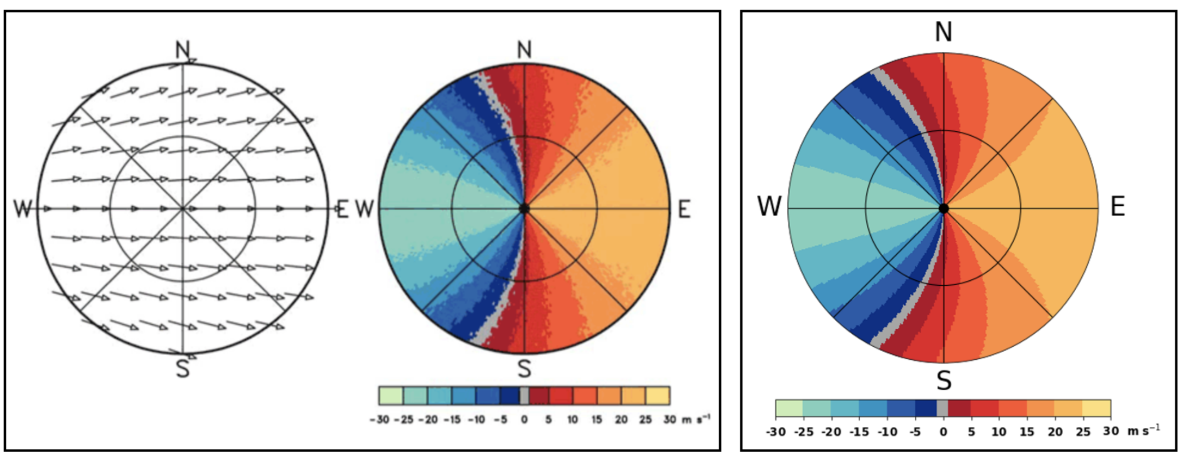

Figure A.3: (**Left**) Doppler velocity pattern corresponding to a horizontal flow field that is difluent with the same speed (23 m s^{-1} or 45 kt) at all heights. Negative (positive) Doppler velocities represent flow toward (away from) the radar. Radar location is at the centre of the display. Caption and Figure taken from (NOAA, 2007). (**Right**) Recreation of this wind field using Python.

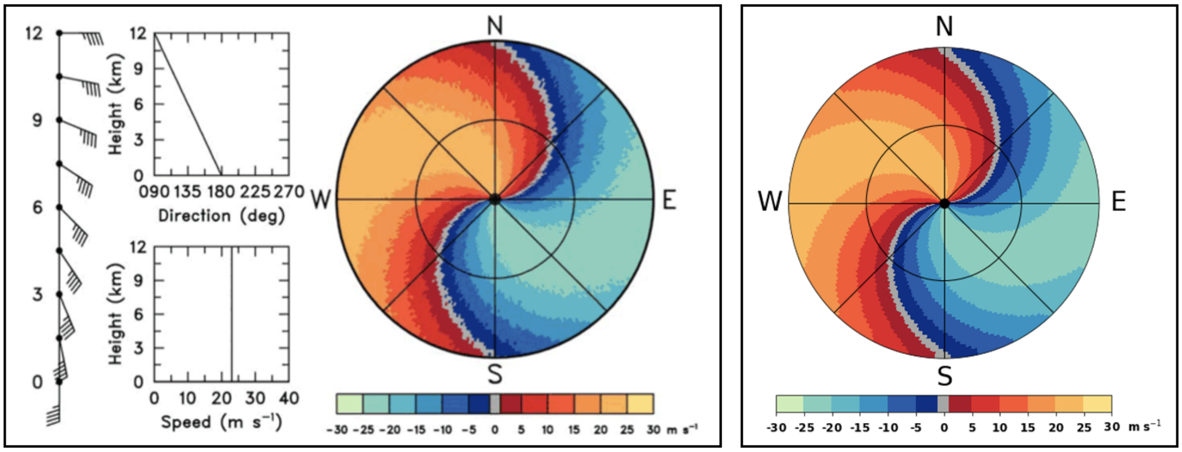

Figure A.4: (**Left**) Doppler velocity pattern corresponding to a vertical wind profile with constant wind speed (23 m s^{-1} or 45 kt) and wind direction backing from southerly to easterly with height. Negative (positive) Doppler velocities represent flow toward (away from) the radar. Radar location is at the centre of the display. Caption and Figure taken from (NOAA, 2007). (**Right**) Recreation of this wind field using Python.

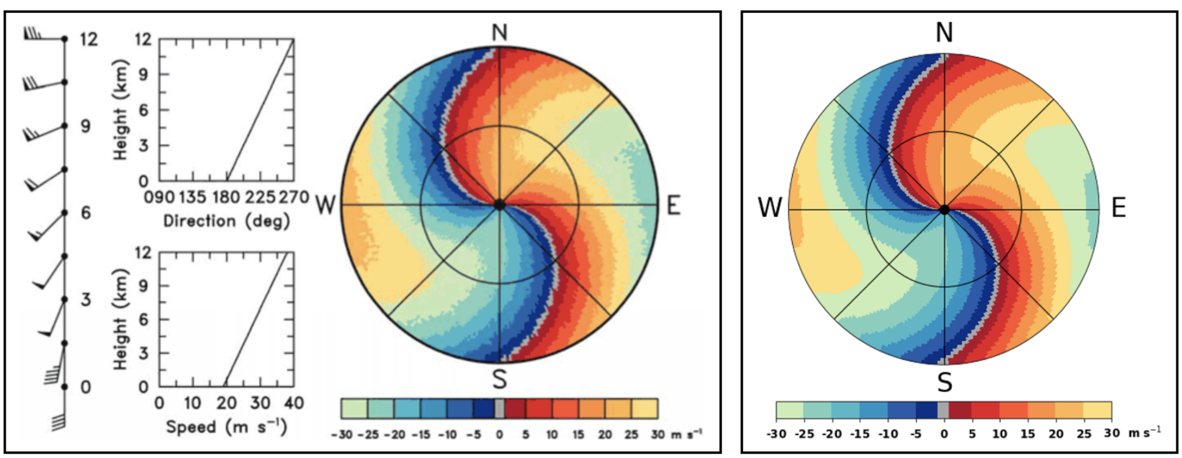

Figure A.5: (**Left**) Doppler velocity pattern corresponding to a vertical wind profile where wind speed increases from 19 to 38 m s^{-1} (74 kt) and direction veers from southerly to westerly with height. Negative (positive) Doppler velocities represent flow toward (away from) the radar. Note that Doppler velocities exceeding ±30 m s^{-1} are aliased. Caption and Figure taken from (NOAA, 2007). (**Right**) Recreation of this wind field using Python.

A.2 Testing the Model with Doppler Radar

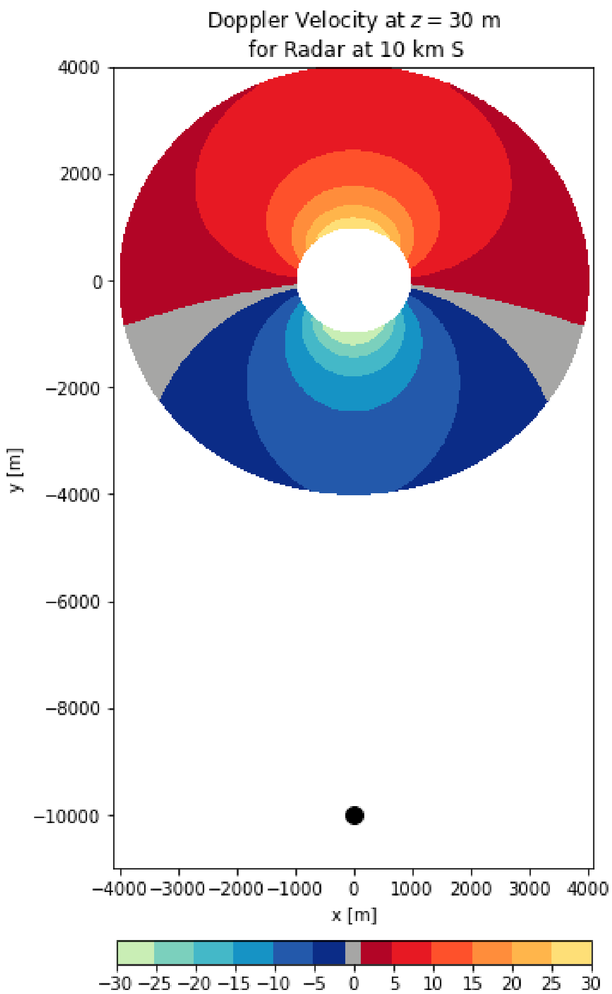

Figure A.6: Doppler velocity of the model as depicted by a radar located 10 km to the south of the centre of the model. The radar position in relation to the model downburst outflow is marked by a black dot.

Appendix B

PyDDA Testing

B.1 Testing the Individual Virtual Radar

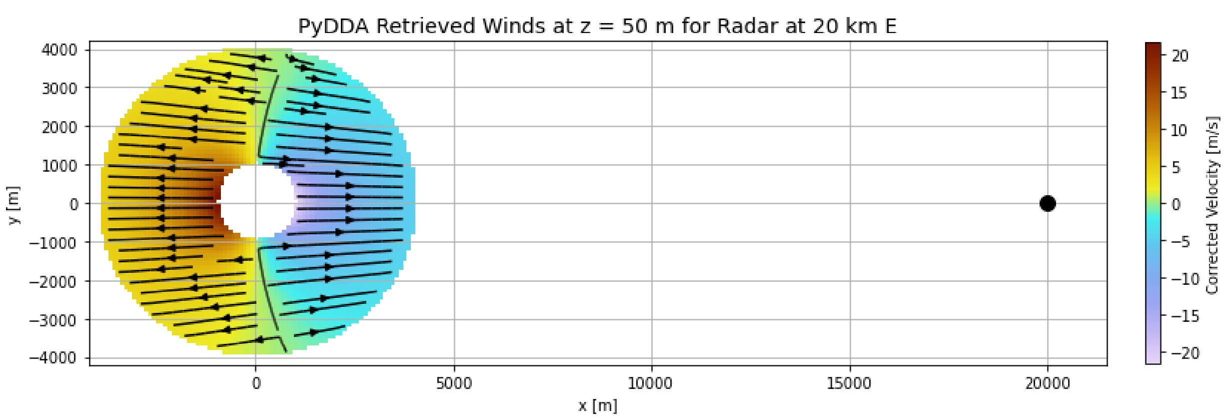

Figure B.1: PyDDA retrieval for one radar located 20 km to the east of the centre of the model downburst outflow. The radar position in relation to the centre of the model downburst outflow are marked by black dots.

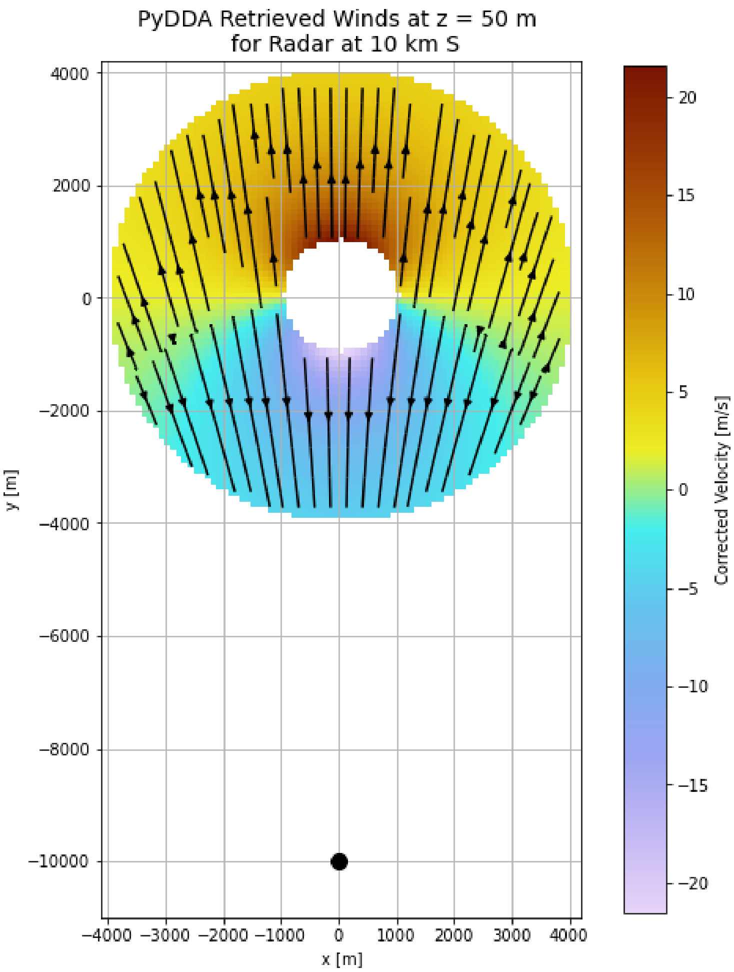

Figure B.2: PyDDA retrieval for one radar located 10 km to the south of the centre of the model downburst outflow. The radar position in relation to the centre of the model downburst outflow are marked by black dots.

B.2 Testing PyDDA with Two Radars

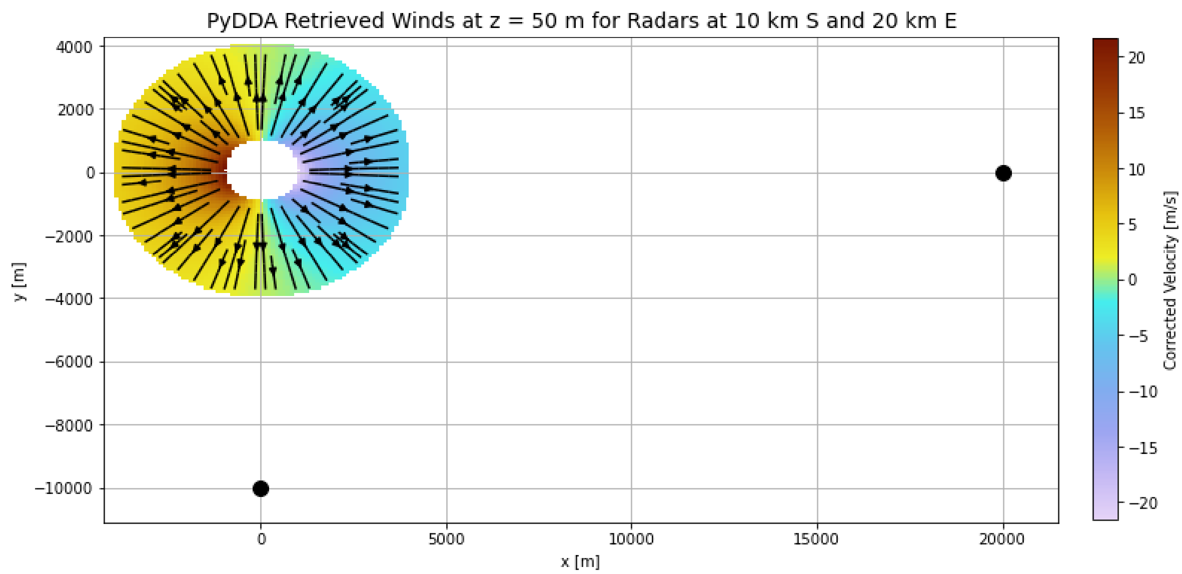

Figure B.3: PyDDA retrieval for two radars, one 10 km to the south and 20 km to the east of the centre of the model downburst outflow. The radar positions in relation to the centre of the model downburst outflow are marked by black dots.